

1 **Probabilistic Hierarchical Interpolation and Interpretable Configuration for Flood Prediction**

2 Mostafa Saberian¹, Vidya Samadi^{2*}, Ioana Popescu³
3 1. The Glenn Department of Civil Engineering, Clemson University, Clemson, SC
4 2. Department of Agricultural Sciences, Clemson University, Clemson, SC.
5 3. Department of Hydroinformatics and Socio-Technical Innovation, IHE Delft Institute for Water
6 Education, Delft, the Netherlands

7 *Corresponding author: samadi@clemson.edu

Formatted: Font: 11 pt

Formatted: Font: 11 pt

8 **Abstract**

9 The last few years have witnessed the rise of Neural-neural Networks-networks (NNs) applications for
10 hydrological time series modeling. By virtue of their capabilities, NN models can achieve unprecedented
11 levels of performance when learn how to solve increasingly complex rainfall-runoff processes via data,
12 making them pivotal for the development of computational hydrologic tasks such as flood predictions. The
13 NN models should, in order to be considered practical, provide a probabilistic understanding of the model
14 mechanisms and predictions and hints on what could perturb the model. In this paper, we developed two
15 probabilistic NN models, i.e., Neural Hierarchical Interpolation for Time Series Forecasting (N-HiTS) and
16 Network-Based Expansion Analysis for Interpretable Time Series Forecasting (N-BEATS) and
17 benchmarked them with long short-term memory (LSTM) for flood prediction across two headwater
18 streams in Georgia and North Carolina, USA. To generate a probabilistic prediction, a Multi-Quantile Loss
19 was used to assess the 95th percentile prediction uncertainty (95PPU) of multiple flooding events. We
20 conducted extensive flood prediction experiments demonstrating the advantages of hierarchical
21 interpolation and interpretable architecture, where both N-HiTS and N-BEATS provided an average
22 accuracy improvement of almost 5% (NSE) over the LSTM benchmarking model. On a variety of flooding
23 events ~~with different timing and magnitudes~~, both N-HiTS and N-BEATS demonstrated significant
24 performance improvements over the LSTM benchmark and showcased their probabilistic predictions by
25 specifying a likelihood parameter.

26 **Keywords:** Probabilistic Flood Prediction; Neural Networks; N-HiTS; N-BEATS; LSTM; Headwater
27 Stream.

28 **Key Points**

29 • N-HiTS and N-BEATS predictions reflect interpretability and hierarchical representations of data
30 to reduce neural network complexities.

31 • Both N-HiTS and N-BEATS models outperformed the LSTM in mathematically defining
32 uncertainty bands.

33 • Predicting the magnitude of the recession curve of flood hydrographs was particularly challenging
34 for all models.

35 **Plain Language Summary**

36 Recent progress in neural network accelerated improvements in the performance of catchment modeling
37 systems. Yet flood modeling remains a very difficult task. Focusing on two headwater streams, this paper
38 developed Neural Hierarchical Interpolation for Time Series Forecasting (N-HiTS) and Network-Based
39 Expansion Analysis for Interpretable Time Series Forecasting (N-BEATS) and benchmarked them with
40 long short-term memory (LSTM) to predict multiple flooding events. Analysis suggested that both N-HiTS
41 and N-BEATS outperformed LSTM for short-term (1 hour) flood predictions. We demonstrated how the
42 proposed N-HiTS and N-BEATS architectures can be augmented with uncertainty and sensitivity
43 approaches to provide skilled flood predictions that are interpretable without considerable loss in accuracy.

44

45 **1. Introduction**

46 The last few years have been characterized by an upsurge in the Neural neural Networks networks (NN)
47 applications in hydrology models. As opaque NN models are increasingly being employed to make
48 important predictions in hydrological systems predictions, the demand for creating legitimate NN models is
49 increasing in the hydrology community. However, maintaining coherence while producing accurate
50 predictions can be a challenging problem (Olivares et al., 2024). There is a general agreement on the
51 importance of providing probabilistic NN prediction (Samadi et al., 2020), especially in the case of flood
52 prediction (Martinaitis et al., 2023).

53 Flood occurrences have witnessed an alarming surge in frequency and severity globally. Jonkman (2005)
54 studied a natural disaster database (EM-DAT, 2023) and reported that over 27 years, more than 175000
55 people died, and close to 2.2 billion were affected directly by floods worldwide. These numbers are likely
56 an underestimation due to unreported events (Nevo et al., 2022). In addition, the United Nations Office for
57 Disaster Risk Reduction reported that flooding has been the most frequent, widespread weather-related
58 natural disaster since 1995, claiming over 600,000 lives, affecting around 4 billion people globally, and
59 causing annual economic damage of more than 100 billion USD (UNISDR, 2015). This escalating trend
60 has necessitated the need for better flood prediction and management strategies. Scholars have successfully
61 implemented different flood models such as deterministic (e.g.... Roelvink et al., 2009, Thompson and
62 Frazier, 2014; Barnard et al., 2014; Erikson et al., 2018) and physically based flood models (e.g.... Basso et
63 al., 2016; Chen et al., 2016; Pourreza-Bilondi et al., 2017; Saksena et al., 2019; Refsgaard et al., 2021) in
64 various environmental systems over the past several decades. These studies have heightened the need for
65 precise flood prediction, they have also unveiled limitations inherent in existing deterministic and physics-

66 based models. While evidence suggests that both deterministic and physics-based approaches are
67 meaningful and useful (Sukovich et al., 2014; [Zafarmomen et al., 2024](#)), their forecasts rest heavily on
68 imprecise and subjective expert opinion; there is a challenge for setting robust evidence-based thresholds
69 to issue flood warnings and alerts (Palmer, 2012). Moreover, many of these traditional flood models
70 particularly physically explicit models rely heavily on a particular choice of numerical approximation and
71 describe multiple process parameterizations only within a fixed spatial architecture (e.g., Clark et al., 2015).
72 Recent NN models have shown promising results across a large variety of flood modeling applications (e.g.,
73 Nevo et al., 2022; Pally and Samadi, 2022; Dasgupta et al., 2023; Zhang et al., 2023) and encourage the
74 use of such methodologies as core drivers for neural flood prediction (Windheuser et al., 2023).
75 Earlier adaptations of these intelligent techniques showed promising ~~results~~ for flood prediction (e.g., Hsu
76 et al., 1995; Tiwari and Chatterjee, 2010). However, recent efforts have taken NN application to the next
77 level, providing uncertainty assessment (Sadeghi Tabas and Samadi, 2022) and improvements over various
78 spatio-temporal scales, regions, and processes (e.g., Kratzert et al., 2018; Park and Lee, 2023; Zhang et al.,
79 2023). Nevo et al., (2022) were the first scholars who employed long short-term memory (LSTM) for flood
80 stage prediction and inundation mapping, achieving notable success during the 2021 monsoon season. Soon
81 after, Russo et al. (2023) evaluated various NN models for predicting flood depth in urban systems,
82 highlighting the potential of data-driven models for urban flood prediction. Similarly, Defontaine et al.
83 (2023) emphasized the role of NN algorithms in enhancing the reliability of flood predictions, particularly
84 in the context of limited data availability. Windheuser et al., (2023) studied flood gauge height forecasting
85 using images and time series data for two gauging stations in Georgia, USA. They used multiple NN models
86 such as Convolutional Neural Network (ConvNet/CNN) and LSTM to forecast floods in near real-time (up
87 to 72 hours). In a sequence, Wee et al., (2023) used Impact-Based Forecasting (IBF) to propose a Flood
88 Impact-Based Forecasting system (FIBF) using flexible fuzzy inference techniques, aiding decision-makers
89 in a timely response. Zou et al. (2023) proposed a Residual LSTM (ResLSTM) model to enhance and
90 address flood prediction gradient issues. They integrated Deep Autoregressive Recurrent (DeepAR) with
91 four recurrent neural networks (RNNs), including ResLSTM, LSTM, Gated Recurrent Unit (GRU), and
92 Time Feedforward Connections Single Gate Recurrent Unit (TFC-SGRU). [They and](#) showed that
93 ResLSTM achieved superior accuracy. While these studies reported the superiority of NN models for flood
94 modeling, they highlighted a number of challenges, notably (i) the limited capability of proposed NN
95 models to capture the spatial variability and magnitudes of extreme data over time, (ii) the lack of a
96 sophisticated mechanism to capture different flood magnitudes and synthesize the prediction, and (iii)
97 inability of the NN models to process data in parallel and capture the relationships between all elements in
98 a sequential manner.

99 Recent advances in neural time series forecasting showed promising results that can be used to address the
100 above challenges for flood prediction. Recent techniques include the adoption of the attention mechanism
101 and Transformer-inspired approaches (Fan et al. 2019; Alaa and van der Schaar 2019; Lim et al. 2021)
102 along with attention-free architectures composed of deep stacks of fully connected layers (Oreshkin et al.
103 2020). All of these approaches are relatively easy to scale up in terms of flood magnitudes (small to major
104 flood predictions), compared to LSTM and have proven to be capable of capturing spatiotemporal
105 dependencies (Challu et al., 2022). In addition, these architectures can capture input-output relationships
106 implicitly while they tend to be more computationally efficient. Many state-of-the-art NN approaches for
107 flood forecasting have been established based on LSTM. There are cell states in the LSTM networks that
108 can be interpreted as storage capacity often used in flood generation schemes. In LSTM, the updating of
109 internal cell states (or storages) is regulated through a number of gates: the first gate regulates the storage
110 depletion, the second one regulates storage fluctuations, and the third gate regulates the storages outflow
111 (Tabas and Samadi, 2022). The elaborate gated design of the LSTM partly solves the long-term dependency
112 problem in flood time series prediction (Fang et al., 2020), although, the structure of LSTMs is designed in
113 a sequential manner that cannot directly connect two nonadjacent portions (positions) of a time series. ~~This
114 indicates the fact that data dependencies can flow from left to right, rather than in both directions as in the
115 ease of the attention based and Transformer approaches.~~
116 In this paper, we ~~take a step in this direction by developing developed~~ attention-free architecture, i.e. Neural
117 Hierarchical Interpolation for Time Series Forecasting (N-HiTS; Challu et al., 2022) and Network-Based
118 Expansion Analysis for Interpretable Time Series Forecasting (N-BEATS; Oreshkin et al., 2020) and
119 benchmarked these models with LSTM for flood prediction. We developed fully connected N-BEATS and
120 N-HiTS architectures using multi-rate data sampling, synthesizing the flood prediction outputs via multi-
121 scale interpolation.
122 We implemented all algorithms for flood prediction on two headwater streams i.e., the Lower Dog River,
123 Georgia, and the Upper Dutchmans Creek, North Carolina, USA. ~~We selected two study areas~~ to ensure
124 that the results are reliable and comparable. The results of N-BEATS and N-HiTS techniques were
125 compared with the benchmarking LSTM to understand how these techniques can improve the
126 representations of rainfall and runoff dispensing over a recurrence process. Notably, this study represents a
127 pioneering effort, as to the best of our knowledge, ~~it this~~ is the first instance in which the application of N-
128 BEATS and N-HiTS algorithms in the field of flood prediction has been explored. The scope of this research
129 will focus on:
130 **(i) Flood prediction in a hierarchical fashion with interpretable outputs:** We built N-BEATS and
131 N-HiTS for flood prediction with a very deep stack of fully connected layers to implicitly capture input-
132 output relationships with hierarchical interpolation capabilities. The predictions also involve programming

Formatted: Font: Bold, Not Italic

133 the algorithms with decreasing complexity and aligning their time scale with the final output through multi-
134 scale hierarchical interpolation and interpretable architecture. Predictions were aggregated in a hierarchical
135 fashion that enabled the building of a very deep neural network with interpretable configurations.

136 **2.(ii) - Uncertainty quantification of the models by employing probabilistic approaches:** a Multi-
137 Quantile Loss (MQL) was used to assess the 95th percentile prediction uncertainty (95PPU) of multiple
138 flooding events. MQL was integrated as the loss function to account for probabilistic prediction. MQL
139 trains the model to produce probabilistic forecasts by predicting multiple quantiles of the distribution of
140 future values.

141 **2.(iii) Exploring headwater stream response to flooding:** Understanding the dynamic response of
142 headwater streams to flooding is essential for managing downstream flood risks. Headwater streams
143 constitute the uppermost sections of stream networks, usually comprising 60% to 80% of a catchment area.
144 Given this substantial coverage and the tendency for precipitation to increase with elevation, headwater
145 streams are responsible for generating and controlling the majority of runoff in downstream portions
146 (MacDonald and Coe, 2007).

147 The remainder of this paper is structured as follows. Section 2 presents the case study and data, NN models,
148 performance metrics, and sensitivity and uncertainty approaches. Section 3 focuses on the results of flood
149 predictions including sensitivity and uncertainty assessment and computation efficiency. Finally, Section 4
150 concludes the paper.

151
152 **2. Methodology**
153 **2.1. Case Study and Data**
154 This research used two headwater gauging stations located at the Lower Dog River watershed, Georgia
155 (GA; USGS02337410, Dog River gauging station), and the Upper Dutchmans Creek watershed, North
156 Carolina (NC; USGS0214269560, Killian Creek gauging station). As depicted in Figures 1 and 2, the Lower
157 Dog River and the Upper Dutchmans Creek watersheds are located in the west and north parts of two
158 metropolitan cities, Atlanta and Charlotte. As shown in Figure 1, the Lower Dog River stream gauge is
159 established southeast of Villa Rica in Carroll County, where the USGS has regularly monitored discharge
160 data since 2007 in 15-minute increments. The Lower Dog River is a stream with a length of 15.7 miles
161 (25.3 km; obtained from the U.S. Geological Survey [USGS] National Hydrography Dataset high-
162 resolution flowline data), an average elevation of 851.94 meters, and the watershed area above this gauging
163 station is 66.5 square miles (172 km²; obtained from the Georgia Department of Natural Resources). This
164 watershed is covered by 15.2% residential area, 14.6% agricultural land, ~~and~~ ~~and~~ ~70% forest (Munn et
165 al., 2020). Killian Creek gauging station at the Upper Dutchmans Creek watershed is established
166 in Montgomery County, ~~North Carolina~~ NC, where the USGS has regularly monitored discharge data since

Formatted: Font: Bold, Not Italic

Formatted: Font: Bold, Not Italic

Formatted: Font: Bold, Not Italic

Formatted: Font: Bold

Formatted: Font: Bold, Not Italic

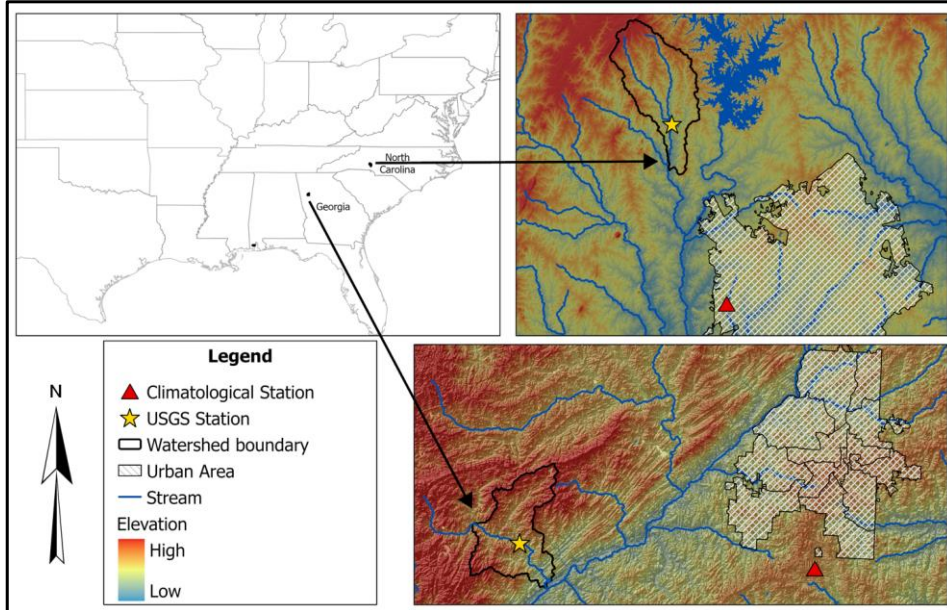
167 1995 in 15-minute increments. The Upper Dutchmans Creek is a stream with a length of 4.9 miles (7.9 km),
168 an average elevation of 642.2 meters (see Table 1), and the watershed area above this gauging station is 4
169 square miles (10.3 km²) with less than 3% residential area and about 93% forested land use (the United
170 States Environmental Protection Agency).

171
172 The Lower Dog River has experienced significant flooding in the last decades. For example, in September
173 2009, the creek, along with most of northern GA, experienced heavy rainfall (5 inches, equal to 94 mm).
174 The Lower Dog River, overwhelmed by large amounts of overland flow from saturated ground in the
175 watershed, experienced massive flooding in September 2009 (Gotvald, 2010). The river crested at 33.8 feet
176 (10.3 m) with a peak discharge of 59,900 cfs (1,700 m³/s), nearly six times the 100-year flood level
177 (McCallum and Gotvald, 2010). In addition, Dutchmans Creek has experienced significant flooding in
178 February 2020. According to local news (WCCB Charlotte, 2020), the flood in Gaston County caused
179 significant infrastructure damage and community disruption. Key impacts included the threatened collapse
180 of the Dutchman's Creek bridge in Mt. Holly and the closure of Highway 7 in McAdenville.GA.
181

182 Table 1. The Lower Dog River and Upper Dutchmans Creek's physical characteristics.

Watershed	USGS Station ID Number	Average Elevation (m)	Stream Length (km)	Watershed area (km ²)
Lower Dog River watershed, GA	USGS02337410	851.9	25.3	172
Upper Dutchmans Creek watershed, NC	USGS0214269560	642.2	7.9	10.3

183



184
185 Figure 1. The Lower Dog River and The Upper Dutchmans Creek watersheds are located in GA and NC.
186 The proximity of the watersheds to Atlanta and Charlotte (urban area) are also displayed on the map.

187
188 To provide the meteorological forcing data, i.e., precipitation, temperature, and humidity, were extracted
189 from the National Oceanic and Atmospheric Administration's (NOAA) Local Climatological Data
190 (LCD). We used the NOAA precipitation, temperature, and humidity data of Atlanta Hartsfield Jackson
191 International Airport and Charlotte Douglas Airport stations as an input variable for neural network
192 algorithms. The data has been monitored since January 1, 1948, and July 22, 1941, with an hourly interval
193 which was used as an input variable for constructing neural networks.

194 To fill in the missing values in the data, we used the spline interpolation method. We applied this method
195 to fill the gaps in time series data, although the missing values were insignificant (less than 1%). In addition,
196 we employed the Minimum Inter-Event Time (MIT) approach to precisely identify and separate individual
197 storm events. The MIT-based event delineation is pivotal for accurately defining storm events. This method
198 allowed us to isolate discrete rainfall episodes, aiding a comprehensive analysis of storm events. Moreover,
199 it provided a basis for event-specific examination of flood responses, such as initial condition and cessation
200 (loss), runoff generation, and runoff dynamics.

202 The hourly rainfall dataset consists of distinct rainfall occurrences, some consecutive and others clustered
203 with brief intervals of zero rainfall. As these zero intervals extend, we aim to categorize them into distinct
204 events. It's worth noting that even within a single storm event, we often encounter short periods of no
205 rainfall, known as intra-storm zero values. In the MIT method, we defined a storm event as a discrete rainfall
206 episode surrounded by dry periods both preceding and following it, determined by an MIT (Asquith et al.,
207 2005; Safaei-Moghadam et al., 2023). There are many means to determine an MIT value. One practical
208 approximation is using serial autocorrelation between rainfall occurrences. MIT approach uses
209 autocorrelation that measures the statistical dependency of rainfall data at one point in time with data at
210 earlier, or lagged times within the time series. The lag time represents the gap between data points being
211 correlated. When the lag time is zero, the autocorrelation coefficient is unity, indicating a one-to-one
212 correlation. As the lag time increases, the statistical correlation diminishes, converging to a minimum value.
213 This signifies the fact that rainfall events become progressively less statistically dependent or, in other
214 words, temporally unrelated. To pinpoint the optimal MIT, we analyzed the autocorrelation coefficients for
215 various lag times, observing the point at which the coefficient approaches zero. This lag time signifies the
216 minimum interval of no rainfall, effectively delineating distinct rainfall events.

217 **2.2. Neural NetworkNN Algorithms**

218 **2.2.1. LSTM**

219 LSTM is an RNN architecture widely used as a benchmark model for flood neural time series
220 modeling. LSTM networks are capable of selectively learning order dependence in sequence prediction
221 problems (Sadeghi Tabas and Samadi, 2022). These networks are powerful because they can capture the
222 temporal features, especially the long-term dependencies (Hochreiter et al., 2001), and are independent of
223 the length of the input data sequences meaning that each sample is independent from another one.

224 The memory cell state within LSTM plays a crucial role in capturing extended patterns in data, making it
225 well-suited for dynamic time series modeling such as flood prediction. An LSTM cell uses the following
226 functions to compute flood prediction.

$$i_t = \sigma(A_i x_t + B_i h_{t-1} + c_i) \quad (\text{Equation 1})$$

$$f_t = \sigma(A_f x_t + B_f h_{t-1} + c_f) \quad (\text{Equation 2})$$

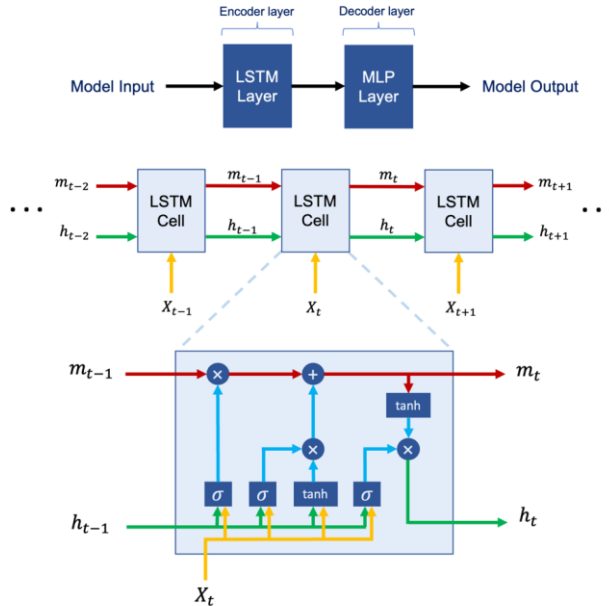
$$o_t = \sigma(A_o x_t + B_o h_{t-1} + c_o) \quad (\text{Equation 3})$$

227 $m_t = f_t \odot m_{t-1} + i_t \odot \tanh(A_g x_t + B_g h_{t-1} + c_g)$ (Equation 4)

228 $h_t = o_t \odot \tanh(m_t)$ (Equation 5)

229 Where x_t and h_t represent the input and the hidden state at time step t , respectively. \odot denotes element-
230 wise multiplication, \tanh stands for the hyperbolic tangent activation function, and σ represents the
231 sigmoid activation function. A , B , and c are trainable weights and biases that undergo optimization during
232 the training process. m_t and h_t are cell states at time step t that are employed in the input processing for
233 the next time step. m_t represents the memory state responsible for preserving long-term information, while
234 h_t represents the memory state preserving short-term information. The LSTM cell consists of a forget gate
235 f_t , an input gate i_t and an output gate o_t and has a cell state m_t . At every time step t , the cell gets the data
236 point x_t with the output of the previous cell h_{t-1} (Windheuser et al., 2023). The forget gate then defines if
237 the information is removed from the cell state, while the input gate evaluates if the information should be
added to the cell state and the output gate specifies which information from the cell state can be used for
the next cells.

238 We used two LSTM layers with 128 cells in the first two hidden layers as encoder layers, which were then
239 connected to two multilayer perceptron (MLP) layers with 128 neurons as decoder layers. The LSTM
240 simulation was performed with these input layers along with the *Adam* optimizer (Kingma and Ba,
241 2014), \tanh activation function, and a single lagged dependent-variable value to train with a learning rate
242 of 0.001. The architecture of the proposed LSTM model is illustrated in Figure 2.



243
244
245
246

Figure 2. The structure of LSTM programmed in this research. We used *tanh* and *sigmoid* as activation functions along with 2 layers of LSTM, 2 layers of MLP, and 128 cells in each layer.

Formatted: Font: 11 pt

2.2.2. N-BEATS

248 N-BEATS is a deep learning architecture based on backward and forward residual links and the very deep
249 stack of fully connected layers specifically designed for sequential data forecasting tasks (Oreshkin et al.,
250 2020). This architecture has a number of desirable properties including interpretability. The N-BEATS
251 architecture distinguishes itself from existing architectures in several ways. First, the algorithm approaches
252 forecasting as a non-linear multivariate regression problem instead of a sequence-to-sequence
253 challenge. Indeed, the core component of this architecture (as depicted in Figure 3) is a fully connected
254 non-linear regressor, which takes the historical data from a time series as input and generates multiple data
255 points for the forecasting horizon. Second, the majority of existing time series architectures are quite limited
256 in depth, typically consisting of one to five LSTM layers. N-BEATS employs the residual principle to stack
257 a substantial number of layers together, as illustrated in Figure 3. In this configuration, the basic block not
258 only predicts the next output but also assesses its contribution to decomposing the input, a concept that is
259 referred to as "backcast" (see Oreshkin et al. 2020).

260
261
262
263

264 The basic building block in the architecture features a fork-like structure, as illustrated in Figure 3 (bottom).
265 The l -th block (for the sake of brevity, the block index l is omitted from Figure 3) takes its respective input,
266 x_l , and produces two output vectors: \hat{x}_l and \hat{y}_l . In the initial block of the model, x_l corresponds to the
267 overall model input, which is a historical lookback window of a specific length, culminating with the most
268 recent observed data point. For the subsequent blocks, x_l is derived from the residual outputs of the
269 preceding blocks. Each block generates two distinct outputs: 1. \hat{y}_l : This represents the forward forecast of
270 the block, spanning a duration of H time units. 2. \hat{x}_l : This signifies the block's optimal estimation of x_l ,
271 which is referred to "backcast." This estimation is made within the constraints of the functional space
272 available to the block for approximating signals (Oreshkin et al., 2020).

273 Internally, the fundamental building block is composed of two elements. The initial element involves a
274 fully connected network, which generates forward expansion coefficient predictors, θ_l^f , and a backward
275 expansion coefficient predictor, θ_l^b . The second element encompasses both backward basis layers, g_l^b , and
276 forward basis layers, g_l^f . These layers take the corresponding forward θ_l^f and backward θ_l^b expansion
277 coefficients as input, conduct internal transformations using a set of basis functions, and ultimately yield
278 the backcast, \hat{x}_l , and the forecast outputs, \hat{y}_l , as previously described by Oreshkin et al. (2020). The
279 following equations describe the first element:

$$h_{l,1} = FC_{l,1}(x_l), \quad h_{l,2} = FC_{l,2}(h_{l,1}), \quad h_{l,3} = FC_{l,3}(h_{l,2}), \quad h_{l,4} = FC_{l,4}(h_{l,3}). \quad (\text{Equation 6})$$

$$\theta_l^b = \text{LINEAR}_l^b(h_{l,4}), \quad \theta_l^f = \text{LINEAR}_l^f(h_{l,4}) \quad (\text{Equation 7})$$

280 The LINEAR layer, in essence, functions as a straightforward linear projection, meaning $\theta_l^f = W_l^f h_{l,4}$. As
281 for the fully connected (FC) layer, it takes on the role of a conventional FC layer, incorporating RELU non-
282 linearity as an activation function.

283 The second element performs the mapping of expansion coefficients θ_l^f and θ_l^b to produce outputs using
284 basis layers, resulting in $\hat{y}_l = g_l^f(\theta_l^f)$ and $\hat{x}_l = g_l^b(\theta_l^b)$. This process is defined by the following equation:

$$\hat{y}_l = \sum_{i=1}^{\dim(\theta_l^f)} \theta_{l,i}^f v_i^f, \quad \hat{x}_l = \sum_{i=1}^{\dim(\theta_l^b)} \theta_{l,i}^b v_i^b \quad (\text{Equation 8})$$

285 Within this context, v_i^f and v_i^b represent the basis vectors for forecasting and backcasting, respectively,
 286 while $\theta_{l,i}^f$ corresponds to the i -th element of θ_l^f .

287 The N-BEATS uses a novel hierarchical doubly residual architecture which is illustrated in Figure 3 (top
 288 and middle). This framework incorporates two residual branches, one traversing the backcast predictions
 289 of each layer, while the other traverses the forecast branch of each layer. The following equation describes
 290 this process:

$$x_l = x_{l-1} - \hat{x}_{l-1} \quad , \quad \hat{y} = \sum_l \hat{y}_l \quad (\text{Equation 9})$$

291 As mentioned earlier, in the specific scenario of the initial block, its input corresponds to the model-level
 292 input x . In contrast, for all subsequent blocks, the backcast residual branch x_l can be conceptualized as
 293 conducting a sequential analysis of the input signal. The preceding block eliminates the portion of the signal
 294 \hat{x}_{l-1} that it can effectively approximate, thereby simplifying the prediction task for downstream blocks.
 295 Significantly, each block produces a partial forecast \hat{y}_l , which is initially aggregated at the stack level and
 296 subsequently at the overall network level, establishing a hierarchical decomposition. The ultimate forecast
 297 \hat{y} is the summation of all partial forecasts (Oreshkin et al., 2020).

298 The N-BEATS model has two primary configurations: generic and interpretable. These configurations
 299 determine how the model structures its blocks and how it processes time series data. In the generic
 300 configuration, the model uses a stack of generic blocks that are designed to be flexible and adaptable to
 301 various patterns in the time series data. Each generic block consists of fully connected layers with ReLU
 302 activation functions. The key characteristic of the generic configuration is its flexibility. Since the blocks
 303 are not specialized for any specific pattern (like trend or seasonality), they can learn a wide range of patterns
 304 directly from the data (Oreshkin et al., 2020). In the interpretable configuration, the model architecture
 305 integrates distinct trend and seasonality components. This involves structuring the basis layers at the stack
 306 level specifically to model these elements, allowing the stack outputs to be more easily understood.

307 **Trend Model:** In this stack $g_{s,l}^b$ and $g_{s,l}^f$ are polynomials of a small degree p , functions that vary slowly
 308 across the forecast window, to replicate monotonic or slowly varying nature of trends:

$$\hat{y}_{s,l} = \sum_{i=0}^p \theta_{s,l,i}^f t^i \quad (\text{Equation 10})$$

309 The time vector $t = [0, 1, 2, \dots, H-2, H-1]^T/H$ is specified on a discrete grid ranging from 0 to
 310 $(H-1)/H$, projecting H steps into the future. Consequently, the trend forecast represented in matrix form is:

$$\hat{y}_{s,l}^{tr} = T \theta_{s,l}^f \quad (\text{Equation 11})$$

311
 312 Where the polynomial coefficients, $\theta_{s,l}^f$, predicted by an FC network at layer l of stack s , are described by
 313 Equations (6) and (7). The matrix T , consisting of powers of t , is represented as $[1, t, \dots, t^p]$. When p is
 314 small, such as 2 or 3, it compels $\hat{y}_{s,l}^{tr}$ to emulate a trend (Oreshkin et al., 2020).

315 Seasonality model: In this stack $g_{s,l}^b$ and $g_{s,l}^f$ are periodic functions, to capture the cyclical and recurring
 316 characteristics of seasonality, such that $y_t = y_{t-\Delta}$, where Δ is the seasonality period. The Fourier series
 317 serves as a natural foundation for modeling periodic functions:

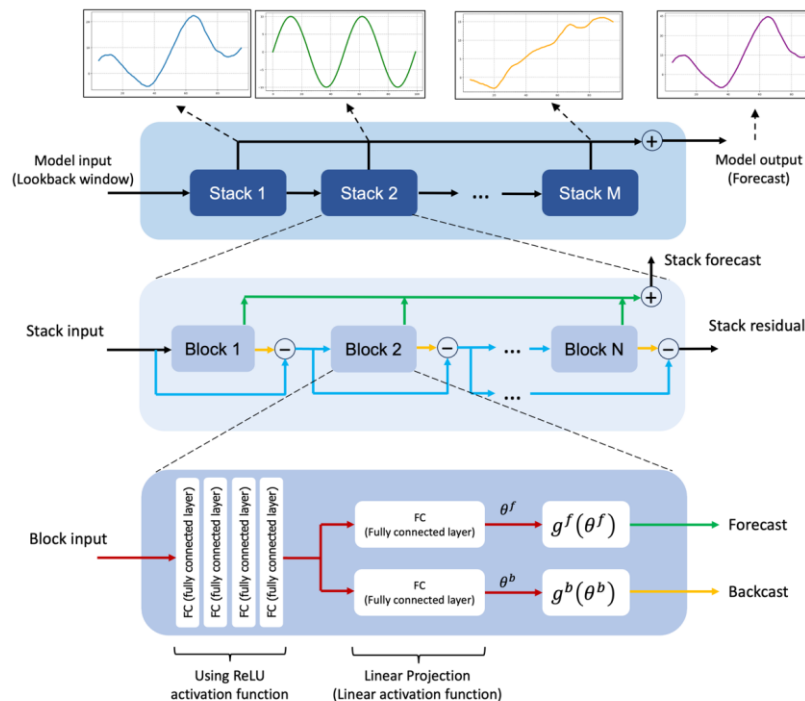
$$\hat{y}_{s,l} = \sum_{i=0}^{\frac{H}{2}-1} \theta_{s,l,i}^f \cos(2\pi i t) + \theta_{s,l,i+\lceil H/2 \rceil}^f \sin(2\pi i t) \quad (\text{Equation 12})$$

318
 319 Consequently, the seasonality forecast is represented in the following matrix form:

$$\hat{y}_{s,l}^{seas} = S \theta_{s,l}^f \quad (\text{Equation 13})$$

$$S = [1, \cos(2\pi t), \dots, \cos\left(2\pi \left[\frac{H}{2}-1\right] t\right), \sin(2\pi t), \dots, \sin\left(2\pi \left[\frac{H}{2}-1\right] t\right)] \quad (\text{Equation 14})$$

320
 321 Where the Fourier coefficients $\theta_{s,l}^f$, that predicted by an FC network at layer l of stack s , are described by
 322 Equations (6) and (7). The matrix S represents sinusoidal waveforms. As a result, the forecast $\hat{y}_{s,l}^{seas}$
 323 becomes a periodic function that imitates typical seasonal patterns (Oreshkin et al., 2020).



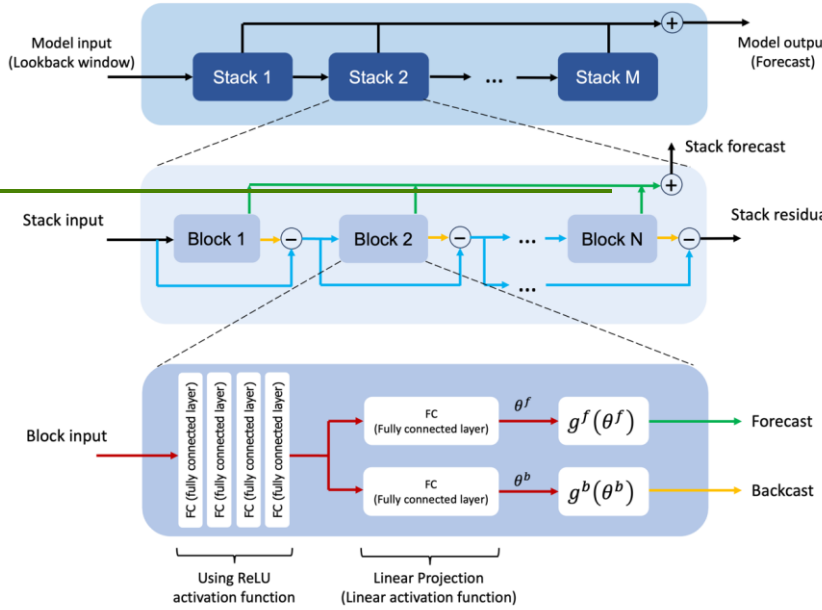


Figure 3. The N-BEATS modeling structure used in this research.

Formatted: Font: 11 pt

325
326
327

328 **2.2.3. N-HiTS**

329 N-HiTS builds upon the N-BEATS architecture but with improved accuracy and computational efficiency
330 for long-horizon forecasting. N-HiTS utilizes multi-rate sampling and multi-scale synthesis of forecasts,
331 leading to a hierarchical forecast structure that lowers computational demands and improves prediction
332 accuracy (Challu et al., 2022).

333 Like N-BEATS, N-HiTS employs local nonlinear mappings onto foundational functions within numerous
334 blocks. Each block includes an MLP that generates backcast and forecast output coefficients. The backcast
335 output refines the input data for the following blocks, and the forecast outputs are combined to generate the
336 final prediction. Blocks are organized into stacks, with each stack dedicated to grasping specific data
337 attributes using its own distinct set of functions. The network's input is a sequence of L lags (look-back
338 period), with S stacks, each containing B blocks (Challu et al., 2022).

339 In each block, a *MaxPool* layer with varying kernel sizes (k_l) is employed at the input, enabling the block
 340 to focus on specific input components of different scales. Larger kernel sizes emphasize the analysis of
 341 larger-scale, low-frequency data, aiding in improving long-term forecasting accuracy. This approach,
 342 known as multi-rate signal sampling, alters the effective input signal sampling rate for each block's MLP
 343 (Challu et al., 2022).

344 Additionally, multi-rate processing has several advantages. It reduces memory usage, computational
 345 demands, the number of learnable parameters, and helps prevent overfitting, while preserving the original
 346 receptive field. The following operation is applicable to the input $y_{t-L:t,l}$ of each block, with the first block
 347 ($l = 1$) using the network-wide input, where $y_{t-L:t,1} \equiv y_{t-L:t}$.

$$y_{t-L:t,l} = \text{MaxPool} (y_{t-L:t,l}, k_l) \quad (\text{Equation 15})$$

348 In many multi-horizon forecasting models, the number of neural network predictions matches the horizon's
 349 dimensionality, denoted as H . For instance, in N-BEATS, the number of predictions $|\theta_l^f| = H$. This results
 350 in a significant increase in computational demands and an unnecessary surge in model complexity as the
 351 horizon H becomes larger (Challu et al., 2022).

352 To address these challenges, N-HiTS proposes the use of temporal interpolation. This model manages the
 353 parameter counts per unit of output time ($|\theta_l^f| = |r_l H|$) by defining the dimensionality of the interpolation
 354 coefficients with respect to the expressiveness ratio r_l . To revert to the original sampling rate and predict
 355 all horizon points, this model employs temporal interpolation through the function g :

$$\hat{y}_{\tau,l} = g(\tau, \theta_l^f), \quad \forall \tau \in \{t+1, \dots, t+H\}, \quad (\text{Equation 16})$$

$$\tilde{y}_{\tau,l} = g(\tau, \theta_l^b), \quad \forall \tau \in \{t-L, \dots, t\}, \quad (\text{Equation 17})$$

$$g(\tau, \theta) = \theta[t_1] + \left(\frac{\theta[t_2] - \theta[t_1]}{t_2 - t_1} \right) (\tau - t_1) \quad (\text{Equation 18})$$

$$t_1 = \arg \min_{t \in \tau: t \leq \tau} \tau - t, \quad t_2 = t_1 + 1/r_l \quad (\text{Equation 19})$$

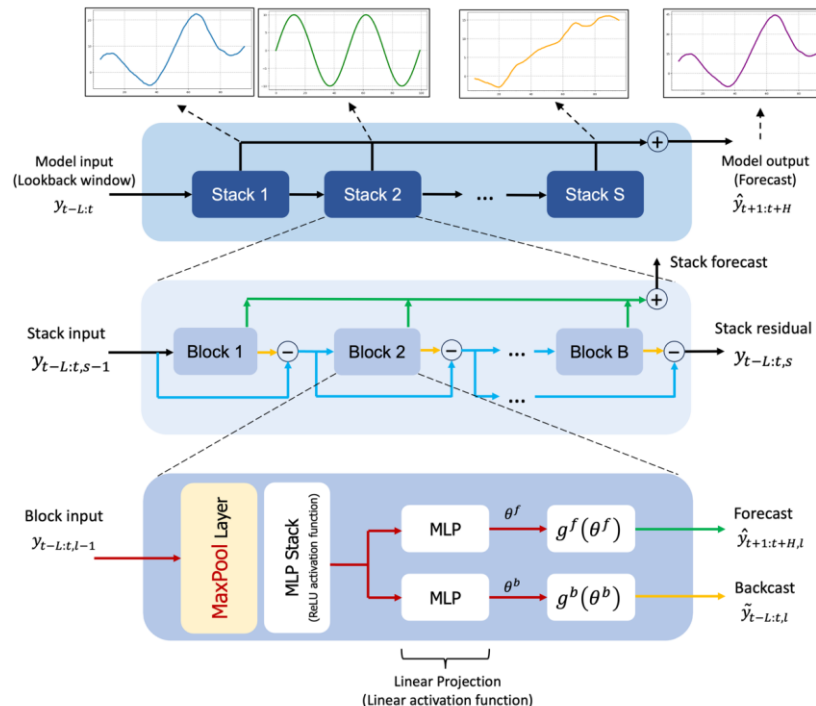
356 The hierarchical interpolation approach involves distributing expressiveness ratios over blocks, integrated
 357 with multi-rate sampling. Blocks closer to the input employ more aggressive interpolation, generating lower
 358 granularity signals. These blocks specialize in analyzing more aggressively subsampled signals. The final
 359 hierarchical prediction, $\hat{y}_{t+1:t+H}$, is constructed by combining outputs from all blocks, creating

360 interpolations at various time-scale hierarchy levels. This approach maintains a structured hierarchy of
361 interpolation granularity, with each block focusing on its own input and output scales (Challu et al., 2022).

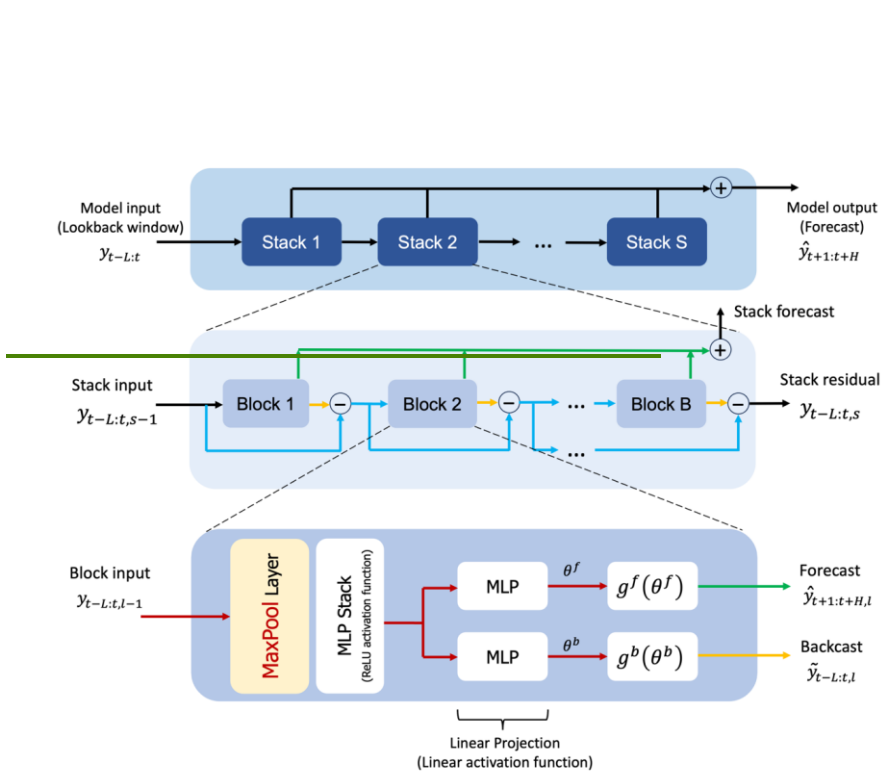
362 To manage a diverse set of frequency bands while maintaining control over the number of parameters,
363 exponentially increasing expressiveness ratios are recommended. As an alternative, each stack can be
364 dedicated to modeling various recognizable cycles within the time series (e.g., weekly, or daily) employing
365 matching r_l . Ultimately, the residual obtained from backcasting in the preceding hierarchy level is
366 subtracted from the input of the subsequent level, intensifying the next-level block's attention on signals
367 outside the previously addressed band (Challu et al., 2022).

$$\hat{y}_{t+1:t+H} = \sum_{l=1}^L \hat{y}_{t+1:t+H,l} \quad (\text{Equation 20})$$

$$y_{t-L:t,l+1} = y_{t-L:t,l} - \tilde{y}_{t-L:t,l} \quad (\text{Equation 21})$$



368



369
370
371
372

Figure 4. The structure of N-HiTS model programmed in this study. The architecture includes several Stacks, each Stack includes several Block, where each block consists of a MaxPool layer and a multi-layer which learn to produce coefficients for the backcast and forecast outputs of its basis.

373 **2.3. Performance Metrics**

374 To comprehensively evaluate the accuracy of flood predictions, we utilized a suite of metrics, including
375 Nash-Sutcliffe Efficiency (NSE; [Nash and Sutcliffe, 1970](#)), persistent Nash-Sutcliffe Efficiency (persistent-
376 NSE), [Kling-Gupta efficiency \(KGE; Gupta et al. 2009\)](#), Root Mean Square Error (RMSE), Mean
377 Absolute Error (MAE), Peak Flow Error (PFE), and Time to Peak Error (TPE; Evin et al., 2023; Lobjigeois
378 et al., 2014). These metrics collectively facilitate a rigorous assessment of the model's performance in
379 reproducing the magnitude of observed peak flows and the shape of the hydrograph.

380 [The Nash-Sutcliffe model efficiency coefficient \(NSE; Nash and Sutcliffe, 1970\)](#) measures the model's
381 ability to explain the variance in observed data and assesses the goodness-of-fit by comparing the observed
382 and simulated hydrographs. In hydrological studies, the NSE index is a widely accepted measure for
383 evaluating the fitting quality of models (McCuen et al., 2006). It is calculated as:

$$NSE = 1 - \frac{\sum_{i=1}^n (Q_{s_i} - Q_{o_i})^2}{\sum_{i=1}^n (Q_{o_i} - \bar{Q}_o)^2} \quad (\text{Equation 22})$$

384 Where Q_{o_i} represents observed value at time i , Q_{s_i} represents simulated value at time i , \bar{Q}_o is the mean
 385 observed values and n is the number of data points. An NSE value of 1 indicates a perfect match between
 386 the observed and modeled data, while lower values represent the degree of departure from a perfect fit.

387 As the models are designed to predict one hour ahead, the persistent-NSE is essential for evaluating their
 388 performance. The standard NSE measures the model's sum of squared errors relative to the sum of squared
 389 errors when the mean observation is used as the forecast value. In contrast, persistent-NSE uses the most
 390 recent observed data as the forecast value for comparison (Nevo et al., 2022). The persistent-NSE is
 391 calculated as:

$$persistent\text{-}NSE = 1 - \frac{\sum_{i=1}^n (Q_{s_i} - Q_{o_i})^2}{\sum_{i=1}^n (Q_{o_i} - Q_{o_{i-1}})^2} \quad (\text{Equation 23})$$

392 Where Q_{o_i} represents the observed value at time i , Q_{s_i} represents the simulated value at time i , $Q_{o_{i-1}}$ is the
 393 observed value at the last time step ($i - 1$) and n is the number of data points.

394 The KGE is a widely used performance metric in hydrological modeling and combines multiple aspects of
 395 model performance, including correlation, variability bias, and mean bias. The KGE metric is calculated
 396 using the following equation:

$$KGE = 1 - \sqrt{(r - 1)^2 + (\alpha - 1)^2 + (\beta - 1)^2} \quad (\text{Equation 24})$$

397 Where r represents Pearson correlation coefficient between observed Q_o and simulated Q_s values.
 398 α represents bias ratio, calculated as $\alpha = \frac{\mu_s}{\mu_o}$ where μ_s and μ_o are the means of simulated and observed data,
 399 respectively. β represents variability ratio, calculated as $\beta = \frac{\sigma_s/\mu_s}{\sigma_o/\mu_o}$ where σ_s and σ_o are the standard
 400 deviations of simulated and observed data, respectively.

401 RMSE quantifies the average magnitude of errors between observed and modeled values, offering insights
 402 into the absolute goodness-of-fit, while MAE is a measure of the average absolute difference between the
 403 modeled values and the observed values and provides a measure of the average magnitude of errors. RMSE
 404 is calculated as:

$$RMSE = \sqrt{\frac{1}{n} \sum_{i=1}^n (Q_{o_i} - Q_{s_i})^2} \quad (\text{Equation } \underline{\underline{2425}})$$

405 and MAE is calculated as:

$$MAE = \frac{1}{n} \sum_{i=1}^n |Q_{o_i} - Q_{s_i}| \quad (\text{Equation } \underline{\underline{2526}})$$

406 Where Q_{o_i} represents observed value at time i , Q_{s_i} represents simulated value at time i , and n is the number
407 of data points. RMSE and MAE provide information about the magnitude of modeling errors, with smaller
408 values indicating a better model fit.

409 PFE quantifies the magnitude disparity between observed and modeled peak flow values. The PFE metric
410 is defined as:

$$PFE = \frac{|Q_{o_{max}} - Q_{s_{max}}|}{Q_{o_{max}}} \quad (\text{Equation } \underline{\underline{2627}})$$

411 Where $Q_{o_{max}}$ represents the observed peak flow value, and $Q_{s_{max}}$ signifies the simulated peak flow value.
412 The PFE metric, expressed as a dimensionless value, provides a quantitative measure of the relative error
413 in predicting peak flow magnitudes concerning the observed values. A smaller PFE denotes more accurate
414 modeling of peak flow magnitudes, with a value of zero indicating a perfect match.

415 TPE assesses the temporal alignment of peak flows in the observed and modeled hydrographs. The TPE
416 metric is computed as:

$$TPE = |T_{o_{max}} - T_{s_{max}}| \quad (\text{Equation } \underline{\underline{2728}})$$

417 Where $T_{o_{max}}$ signifies the time at which the peak flow occurs in the observed hydrograph, and $T_{s_{max}}$
418 represents the time at which the peak flow occurs in the simulated hydrograph. TPE that is measured in
419 units of time (hours), provides insight into the precision of peak flow timing. Smaller TPE values indicate
420 a superior alignment between the observed and modeled peak flow timing, while larger TPE values indicate
421 discrepancies in the temporal occurrence of peak flows.

422 The utilization of these five metrics, PFE, persistent-NSE, TPE, NSE, and RMSE, collectively provides a
423 robust and multifaceted assessment of flood prediction performance. This approach ensures that both the
424 magnitude and timing of peak flows, as well as the overall hydrograph shape, are accurately calibrated and
425 validated.

426 **2.4. Sensitivity and Uncertainty Analysis**

427 When implementing NN models, it's crucial to understand how each parameter affects the model's
428 performance or outputs. To achieve this, we systematically excluded each parameter from the model one
429 by one (the Leave-One-Out method). For each exclusion, we retrained the model without that specific
430 parameter and then tested its performance against a test dataset. This method helps in understanding which
431 parameters are most critical to the model's performance and which ones have a lesser impact. It also allows
432 us to identify any parameters that may be redundant or have little effect on the overall outcome, thus
433 potentially simplifying the model without sacrificing accuracy.

434 In this study, we utilized probabilistic approaches to quantify the uncertainty in flood prediction. This
435 method is rooted in statistical techniques employed for the estimation of unknown probability distributions,
436 with a foundation in observed data. More specifically, we leveraged the Maximum Likelihood Estimation
437 (MLE) approach, which entails the determination of parameter values that optimize the likelihood function.
438 The likelihood function quantifies the probability of parameters taking particular values, given the observed
439 realizations.

440 Within our models, we incorporated the MQL as a probabilistic error metric into the algorithmic
441 architecture. MQL performs an evaluation by computing the average loss for a predefined set of quantiles.
442 This computation is grounded in the absolute disparities between predicted quantiles and their
443 corresponding observed values. By considering multiple quantile levels, MQL provides a comprehensive
444 assessment of the model's ability to capture the distribution of the target variable, rather than focusing
445 solely on point estimates.

446 The MQL metric also aligns closely with the Continuous Ranked Probability Score (CRPS), a standard tool
447 for evaluating predictive distributions. CRPS measures the difference between the predicted cumulative
448 distribution function and the observed values by integrating over all possible quantiles. The limited behavior
449 of MQL serves as an apt metric for assessing the accuracy of predictive distribution \hat{F}_p , facilitated through
450 the Continuous Ranked Probability Score (CRPS). The computation of CRPS involves a numerical
451 integration technique that discretizes quantiles and applies a left Riemann approximation for CRPS integral

452 computation. This process culminates in the averaging of these computations over uniformly spaced
 453 quantiles, providing a robust evaluation of the predictive distribution $\hat{F}_{t,\tau}$

454 To calculate the 95th percentile prediction uncertainty PPU, we utilized the 0.95 quantile level within the
 455 MQL. This quantile level directly corresponds to the 95th percentile of the predicted distribution, providing
 456 an estimate of the 95% confidence interval. By examining the model's performance at this specific quantile,
 457 we effectively assessed its ability to accurately capture the predicted values with 95% confidence.

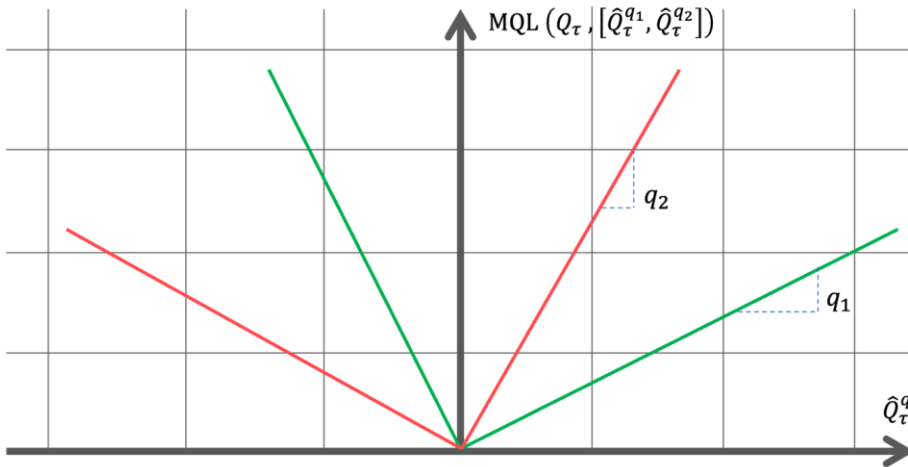
458 Incorporating MQL as a central metric in our study underscores its suitability for probabilistic forecasting,
 459 particularly in the context of uncertainty quantification. Unlike traditional error metrics that focus on point
 460 predictions, MQL captures both central tendencies and variability by penalizing errors symmetrically across
 461 quantiles. This property ensures balanced and reliable assessments of the predictive distribution, ultimately
 462 enhancing the robustness and interpretability of flood prediction models.

$$\text{MQL} (Q_\tau, [\hat{Q}_\tau^{q_1}, \dots, \hat{Q}_\tau^{q_i}]) = \frac{1}{n} \sum_{q_i} \text{QL} (Q_\tau, \hat{Q}_\tau^{q_i}) \quad (\text{Equation } 2829)$$

$$\text{CRPS} (Q_\tau, \hat{F}_\tau) = \int_0^1 \text{QL} (Q_\tau, \hat{Q}_\tau^{q_i}) dq \quad (\text{Equation } 2930)$$

$$\text{QL} (Q_\tau, \hat{Q}_\tau^q) = \frac{1}{H} \sum_{\tau=t+1}^{t+H} ((1-q)(\hat{Q}_\tau^q - Q_\tau) + q(Q_\tau - \hat{Q}_\tau^q)) \quad (\text{Equation } 3031)$$

463 Where Q_τ represents observed value at time τ , \hat{Q}_τ^q represents simulated value at time τ , q is the slope of the
 464 quantile loss, and H is the horizon of forecasting.



465
 466 Figure 5. The MQL function which shows loss values for different parameters of q when the true value is
 467 Q_τ .

468 Furthermore, we employed two key indices, the R-factor Factor and the P-Ffactor, to rigorously assess the
 469 quality of uncertainty performance in our hydrological modeling. These metrics are instrumental in
 470 quantifying the extent to which the model's predictions encompass the observed data, thereby providing
 471 valuable insights into the model's predictive accuracy and reliability.

472 The P-factor Factor, or percentage of data within a 95PPU, is the first index used in this assessment. The P-
 473 factor Factor quantifies the percentage of observed data that falls within the 95PPU, providing a measure
 474 of the model's predictive accuracy. The P-factor Factor can theoretically vary from 0% to a maximum of
 475 100%. A P-factor Factor of 100% signifies a perfect alignment between the model's predictions and the
 476 observed data within the uncertainty band. In contrast, a lower P-factor Factor indicates a reduced ability
 477 of the model to predict data within the specified uncertainty range.

$$P - Factor = \frac{Observations bracketed by 95PPU}{Number of observations} \times 100 \quad (\text{Equation } 3432)$$

478 The R-factor Factor can be computed by dividing the average width of the uncertainty band by the standard
 479 deviation of the measured variable. The R-factor Factor, with a minimum possible value of zero, provides a
 480 measure of the spread of the uncertainty relative to the variability of the observed data. Theoretically, the
 481 R-factor Factor spans from 0 to infinity, and a value of zero implies that the model's predictions precisely

482 match the measured data, with the uncertainty band being very narrow in relation to the variability of the
483 observed data.

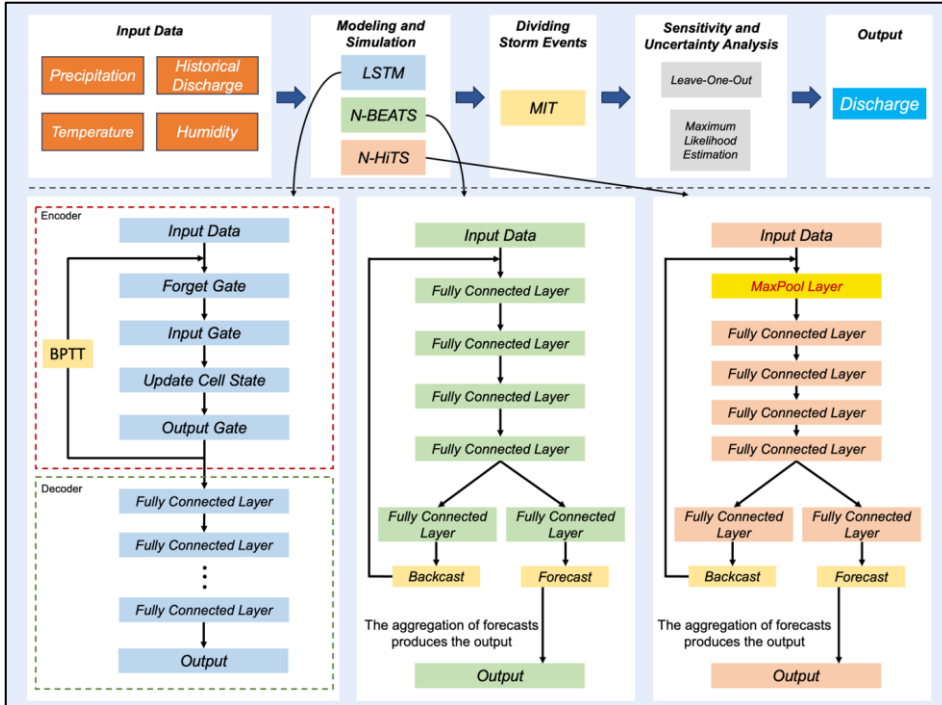
$$R - Factor = \frac{\text{Average width of 95PPU band}}{\text{Standard deviation of measured variables}} \times 100 \quad (\text{Equation 3233})$$

484 In practice, the quality of the model is assessed by considering the 95% prediction band with the highest P-
485 ~~factor~~^{Factor} and the lowest R-~~factor~~^{Factor}. This specific band encompasses the majority of observed
486 records, signifying the model's ability to provide accurate and reliable predictions while effectively
487 quantifying uncertainty. A simulation with a P-~~factor~~^{Factor} of 1 and an R-~~factor~~^{Factor} of 0 signifies an
488 ideal scenario where the model precisely matches the measured data within the uncertainty band
489 (Abbaspour et al., 2007).

490 Figure 6 shows the workflow of programming N-BEATS, N-HiTS, and LSTM for flood prediction. As
491 illustrated, the initial step involved cleaning and preparing the input data, which was then used to feed the
492 models. The workflow for each model and their output generation processes are depicted in Figure 6. We
493 segmented the storm events using the MIT approach, as previously described. Following this, we conducted
494 a sensitivity analysis using the Leave-One-Out method and performed uncertainty analysis using the MLE
495 approach to construct the 95PPU band. This rigorous methodology ensures a robust evaluation of model
496 performance under varying conditions and highlights the models' predictive reliability and resilience. We
497 employed the “NeuralForecast” Python package to develop the N-BEATS, N-HiTS, and LSTM models.
498 This package provides a diverse array of NN models with an emphasis on usability and robustness.

499

500



501

502 Figure 6. The workflow of N-BEATS, N-HiTS, and LSTM implementation. The upper section of the
 503 figure illustrates multiple steps from data preprocessing to model evaluation. The lower section provides a
 504 detailed view of the workflow and implementation for each model, highlighting the specific processes and
 505 methodologies employed in generating the outputs. Backpropagation Through Time (BPTT) trains LSTM
 506 by unrolling the model through time, computing gradients for each time step, and updating weights based
 507 on temporal dependencies.

508

509 **3. Results and Discussion**

510 **3.1. Independent Storms Delineation**

511 MIT's contextual delineation of storm events laid the groundwork for in-depth evaluation of rainfall events,
 512 enabling isolation and separation of rainfall events that led to significant flooding events. The nuanced
 513 outcomes of the MIT assessment contributed significantly to the understanding of rainfall variability and
 514 distribution as the dominant contributor to flood generation.

515 During modeling implementation, the initial imperative was the precise distinction of storm events within
516 the precipitation time series data of each case study. Our findings demonstrate that on average a dry period
517 of 7 hours serves as the optimal MIT time for both of our case studies. This outcome signifies that when a
518 dry interval of more than 7 hours transpires between two successive rainfall events, these subsequent
519 rainfalls should be considered two distinct storm events. This determination underlines the temporal
520 threshold necessary for distinguishing between individual meteorological phenomena in two case studies.

521 **3.2. Hyperparameter Optimization**

522 In the context of hyperparameter optimization, we systematically considered and tuned various
523 hyperparameters for the N-HiTS, N-BEATS, and LSTM. Following extensive exploration and fine-tuning
524 of these hyperparameters, the optimal configurations were identified (see Table 2). For the N-HiTS model,
525 the most favorable outcomes were achieved with the following hyperparameter settings: 2000 epochs,
526 "identity" for scaler type, a learning rate of 0.001, a batch size of 32, input size of 24 hours, "identity" for
527 stack type, 512 units for hidden layers of each stack, step size of 1, MQLoss as loss function, and "ReLU"
528 for the activation function. As shown in Table 2, the N-HiTS model demonstrated superior performance
529 with 4 stacks, containing 2 blocks each, and corresponding coefficients of 48, 24, 12, and 1, showcasing
530 the significance of these settings for flood prediction.

531 This hyperparameter optimization was also conducted for the N-BEATS model. In this model, we
532 considered 2000 epochs, 3 stacks with 2 blocks, "identity" for scaler type, a learning rate of 0.001, a batch
533 size of 32, input size of 24 hours, "identity" for stack type, 512 units for hidden layers of each stack, step
534 size of 1, MQLoss as loss function, and "ReLU" for the activation function.

535 Moreover, the LSTM as a benchmark model yielded its best results with 5000 epochs, an input size of 24
536 hours, "identity" as the scaler type, a learning rate of 0.001, a batch size of 32, and "tanh" as the activation
537 function. Furthermore, the LSTM's hidden state was most effective with two layers containing 128 units,
538 and the MLP decoder thrived with two layers encompassing 128 units. These meticulously optimized
539 hyperparameter settings represent the culmination of efforts to ensure that each model operates at its peak
540 potential, facilitating accurate flood prediction.

541 Table 2. Optimized values for [the models](#) hyperparameters.

Hyperparameter	N-HiTS	N-BEATS	LSTM
Epoch	2000	2000	5000
Scaler type	identity	identity	standard

Learning rate	0.001	0.001	0.001
Batch size	32	32	32
Input size	24 hours	24 hours	24 hours
Stack type	Seasonality, trend, identity, identity	Seasonality, trend, identity	*
Number of units in each hidden layer	512	512	128
Loss function	MQLoss	MQLoss	MQLoss
Activation function	ReLU	ReLU	tanh
Number of stacks	4	3	*
Number of blocks in each stack	2	2	*
Stacks' coefficients	48,24,12,1	*	*

542

*Not applicable

543 In Table 2, "epoch" refers to the number of training steps, and "scaler type" indicates the type of scaler used
 544 for normalizing temporal inputs. The "learning rate" specifies the step size at each iteration while optimizing
 545 the model, and the "batch size" represents the number of samples processed in one forward and backward
 546 pass. The "loss function" quantifies the difference between the predicted outputs and the actual target
 547 values, while the "activation function" determines whether a neuron should be activated. The "stacks'
 548 coefficients" in the N-HITS model control the frequency specialization for each stack, enabling effective
 549 handling of different frequency components in the time series data.

550 Another hyperparameter for all three models is input size, which is a parameter that determines the
 551 maximum sequence length for truncated backpropagation during training and the number of autoregressive
 552 inputs (lags) that the models considered for prediction. Essentially, input size represents the length of the
 553 historical series data used as input to the model. This parameter offers flexibility in the models, allowing
 554 them to learn from a defined window of past observations, which can range from the entire historical dataset
 555 to a subset, tailored to the specific requirements of the prediction task. In the context of flood prediction,
 556 determining the appropriate input size is crucial to adequately capture the meteorological data preceding
 557 the flood event. To address this, we calculated the time of concentration (*TC*) of the watershed system and
 558 set the input size to exceed this duration. According to the Natural Resources Conservation Service (NRCS),
 559 for typical natural watershed conditions, the TC can be calculated from lag time, the time between peak
 560 rainfall and peak discharge, using the formula: *Lag time* = *TC* × 0.6 (NRCS, 2009). Specifically, the

Formatted: Font: Italic

561 average TC in the Lower Dog River watershed and Upper Dutchmans Creek watershed was found to be 19
562 and 22 hours, respectively. As these represent the average TC for our case studies, we selected the 24 hours
563 for input data, slightly longer than the average calculated avaerage TC , ensuring sufficient coverage of
564 relevant meteorological data preceding all flood events. Through hyperparameter optimization, we
565 determined that an input size of 24 hours was optimal for all the models, ensuring sufficient coverage of
566 relevant meteorological data preceding flood events.

Formatted: Font: Italic

Formatted: Font: Italic

Formatted: Font: Italic

567 3.3. Flood Prediction and Performance Assessment

568 In this study, we conducted a comprehensive performance evaluation of N-HiTS, N-BEATS, and
569 benchmarking benchmarked these models with LSTM models, utilizing two case studies: the Lower Dog
570 River and the Upper Dutchmans Creek watersheds. Within these case studies, we trained and validated the
571 models separately for each watershed across a diverse set of storm events from 01/10/2007 to 01/10/2022
572 (15 years) in the Lower Dog River and from 21/12/1994 to 01/10/2022 (27 years) in the Upper Dutchmans
573 Creek. The decision to train separate models for each catchment was made to account for the unique
574 hydrological characteristics and local features specific to each watershed. By training models individually,
575 we aimed to optimize performance by tailoring each model to the distinct rainfall-runoff relationship
576 inherent in each catchment. All algorithms were validated tested using unseen flooding events that occurred
577 between 14/12/2022 and 28/03/2023. In the Dog River gauging station, two winter storms i.e., January 3rd
578 to January 5th, 2023 (Event 1) and February 17th to February 18th, 2023 (Event 2), as well as a spring flood
579 event that occurred during March 26th to March 28th, 2023 (Event 3) were selected for testing.
580 Additionally, three winter flooding events, i.e., December 14th to December 16th, 2022 (Event 4), January
581 25th and January 26th, 2023 (Event 5), and February 11th to February 13th, 2023 (Event 6), were chosen
582 to test the algorithms across the Killian Creek gauging station in the Upper Dutchmans Creek. The rainfall
583 events corresponding to these flooding events were delineated using the MIT technique discussed in Section
584 3.1.

585 Our results for the Lower Dog River case study, explicitly demonstrated the accuracy of both N-HiTS and
586 N-BEATS in generating the winter and spring flood hydrographs compared to the LSTM model across all
587 selected storm events. Although, N-HiTS prediction slightly outperformed N-BEATS during winter
588 prediction (January 3rd to January 5th, 2023). In this event, N-HiTS outperformed N-BEATS with a
589 difference of 11.6% in MAE and 20% in RMSE. The N-HiTS slight outperformance (see Tables 3 and 4)
590 is attributed to its unique structure that allows the model to discern and capture intricate patterns within the
591 data. Specifically, N-HiTS predicted flooding events hierarchically using blocks specialized in different
592 rainfall frequencies based on controlled signal projections, through expressiveness ratios, and interpolation
593 of each block. The coefficients are then used to synthesize backcast through

594 $\tilde{y}_t - L: t, l$ and forecast $(\tilde{y}_{t+1}: t + H, l)$ outputs of the block as a flood value. The coefficients were locally
595 determined along the horizon, allowing N-HiTS to reconstruct nonstationary signals over time.

596 While the N-HiTS emerged as the most accurate in predicting flood hydrograph among the three models,
597 its performance was somehow comparable with N-BEATS. The N-BEATS model exhibited good
598 performance in two case studies. It consistently provided competitive results, demonstrating its capacity to
599 effectively handle diverse storm events and deliver reliable predictions. N-BEATS has a generic and
600 interpretable architecture depending on the blocks it uses. Interpretable configuration sequentially projects
601 the signal into polynomials and harmonic basis to learn trend and seasonality components while generic
602 configuration substitutes the polynomial and harmonic basis for identity basis and larger network's depth.
603 In this study, we used interpretable architecture, as it regularizes its predictions through projections into
604 harmonic and trend basis that is well-suited for flood prediction tasks. Using interpretable architecture,
605 flood prediction was aggregated in a hierarchical fashion. This enabled the building of a very deep neural
606 network with interpretable flood prediction outputs.

607 It is essential to underscore that, despite its strong performance, the N-BEATS model did not surpass the
608 N-HiTS model in terms of NSE, Persistent-NSE, MAE, and RMSE for the Lower Dog River case study.
609 Although both models showed almost the same KGE values. Notably, the N-BEATS model showcased
610 superior results based on the PFE metric, signifying its exceptional capability in accurately predicting flood
611 peaks. However, both N-HiTS and N-BEATS models overestimated the flood peak rate of Event 2 for the
612 Lower Dog River watershed. This event, which occurred from February 17th to 18th, 2023,
613 was flashy, short, and intense proceeded by a prior small rainfall event (from February 12th until February
614 13th) that minimized the rate of infiltration. This flash flood event caused by excessive rainfall in a short
615 period of time (<8 hours) was challenging to predict for ~~both~~-N-BEATS and N-HiTS models. In addition,
616 predicting the magnitude of changes in the recession curve of the third event seems to be a challenge for
617 both models. The specific part of the flood hydrograph after the precipitation event, where flood diminishes
618 during a rainless is dominated by the release of runoff from shallow aquifer systems or natural storages. It
619 seems both models showed a slight deficiency in capturing this portion of the hydrograph when the rainfall
620 amount decreases over time in the Dog River gauging station.

Formatted: Font: Not Bold

621 Conversely, in the Killian Creek gauging station, the N-BEATS model almost emerged as the top performer
622 in predicting the flood hydrograph based on NSE, Persistent-NSE, RMSE, and PFE performance metrics
623 (see Tables 3 and 4). KGE values remained almost the same for both models. AlthoughIn addition, both
624 N-BEATS and N-HiTS slightly overpredicted time to peak values for Event 5. This reflects the fact that
625 when rainfall value varies randomly around zero, it provides less to no information for the algorithms to

626 learn the fluctuations and patterns in time series data. Both N-HiTS and N-BEATS provided comparable
627 results for all events predicted in this study. N-HiTS builds upon N-BEATS by adding a MaxPool layer at
628 each block. Each block consists of an MLP layer that learns to produce coefficients for the backcast and
629 forecast outputs. This subsamples the time series and allows each stack to focus on either short-term or
630 long-term effects, depending on the pooling kernel size. Then, the partial predictions of each stack are
631 combined using hierarchical interpolation. This ability enhances N-HiTS capabilities to produce drastically
632 improved, interpretable, and computationally efficient long-horizon flood predictions.

633 In contrast, the performance of LSTM as a benchmark model lagged behind both N-HiTS and N-BEATS
634 models for all events across two case studies. Despite its extensive applications in various hydrology
635 domains, the LSTM model exhibited comparatively lower accuracy when tasked with predicting flood
636 responses during different storm events. Focusing on NSE, Persistent-NSE, KGE, MAE, RMSE, and PFE
637 metrics, it is noteworthy that all three models, across both case studies, consistently succeeded in capturing
638 peak flow rates at the appropriate timing. All models demonstrated commendable results with respect to
639 the TPE metric. In most scenarios, TPE revealed a value of 0, signifying that the models accurately
640 pinpointed the peak flow rate precisely at the expected time. In some instances, TPE reached a value of 1,
641 showing a deviation of one hour in predicting the peak flow time. This deviation is deemed acceptable,
642 particularly considering the utilization of short, intense rainfall for our analysis.

Formatted: Font: Not Bold
Formatted: Not Highlight

643 Our investigation into the performance of the three distinct forecasting models yielded compelling results
644 pertaining to their ability to generate 95PPU, as quantified by the P-factorFactor and R-factorFactor. These
645 factors serve as critical indicators for assessing the reliability and precision of the uncertainty bands
646 produced by the MLE. Our findings demonstrated that the N-HiTS and N-BEATS models outperformed
647 the LSTM model in mathematically defining uncertainty bands, in terms of R-factorFactor metric. The R-
648 factorFactor, a crucial metric for evaluating the average width of the uncertainty band, consistently favored
649 the N-HiTS and N-BEATS models over their counterparts. This finding was consistent across a diverse
650 range of storm events. In addition, Coupling MLE with the N-HiTS and N-BEATS models demonstrated
651 superior performance in generating 95PPU when assessed through the P-factorFactor metric. The P-factor
652 Factor represents another vital aspect of uncertainty quantification, focusing on the precision of the
653 uncertainty bands.

654
655 Figures 8 and 9 present graphical depictions of the predicted flood with uncertainty assessment for each
656 model as well as Flow Duration Curve (FDC) across two gauging stations. As illustrated, the uncertainty
657 bands skillfully bracketed most of the observational data, reflecting the fact that MLE was successful in

658 reducing errors in flood prediction. FDC analysis also revealed that N-HiTS and N-BEATS models
 659 skillfully predicted the flood hydrograph, however, both models were particularly successful in predicting
 660 moderate to high flood events (1800-6000 and >6000 cfs). In the FDC plots, the x-axis denotes the
 661 exceedance probability, expressed as a percentage, while the y-axis signifies flood in cubic feet per second.
 662 Notably, these plots reveal distinctive patterns in the performance of the N-HiTS, N-BEATS, and LSTM
 663 models. Within the lower exceedance probability range, particularly around the peak flow, the N-HiTS and
 664 N-BEATS models demonstrated a clear superiority over the LSTM model, closely aligning with the
 665 observed data. This observed trend is consistent when examining the corresponding hydrographs. Across
 666 all events, the flood hydrographs generated by N-HiTS and N-BEATS exhibited a closer resemblance to
 667 the observed data, particularly in the vicinity of the peak timing and rate, compared to the hydrographs
 668 produced by the LSTM model. These findings underscore the enhanced predictive accuracy and reliability
 669 of the N-HiTS and N-BEATS models, particularly in predicting moderate to high flood events as well as
 670 critical hydrograph features such as peak flow rate and timing. The alignment of model-generated FDCs
 671 and hydrographs with observed data in the proximity of peak flow further establishes the ~~efficacy~~efficiency
 672 of N-HiTS and N-BEATS in accurately reproducing the dynamics of flood generation mechanisms across
 673 two headwater streams.

674

675 Table 3. ~~Accuracy and uncertainty~~The performance metrics for the Lower Dog River flood predictions.

Model	Performance Metric	Event 1	Event 2	Event 3
N-HiTS	NSE	0.995	0.991	0.992
	Persistent-NSE	0.947	0.931	0.948
	KGE	0.977	0.989	0.976
	RMSE	123.2	27.6	68.5
	MAE	64.1	12.0	37.8
	PFE	0.018	0.051	0.015
	TPE (hours)	0	1	0
N-BEATS	P-Factor	96.9 %	100 %	93.5 %
	R-Factor	0.27	0.40	0.33
	NSE	0.991	0.989	0.993
	Persistent-NSE	0.917	0.916	0.956
	KGE	0.984	0.984	0.98
	RMSE	154.1	30.5	62.5
	MAE	72.6	13.6	35.9

	PFE	0.0005	0.031	0.0002
	TPE (hours)	0	1	0
	P-Factor	87.8 %	100 %	90.3 %
	R-Factor	0.17	0.23	0.24
	NSE	0.756	0.983	0.988
	Persistent-NSE	-1.44	0.871	0.929
	KGE	<u>0.765</u>	<u>0.978</u>	<u>0.971</u>
	RMSE	841.1	37.9	79.5
LSTM	MAE	369.4	18.6	42
	PFE	0.258	0.036	0.016
	TPE (hours)	1	0	0
	P-Factor	81.8 %	93.1 %	96.7 %
	R-Factor	0.37	0.51	0.6

676

677

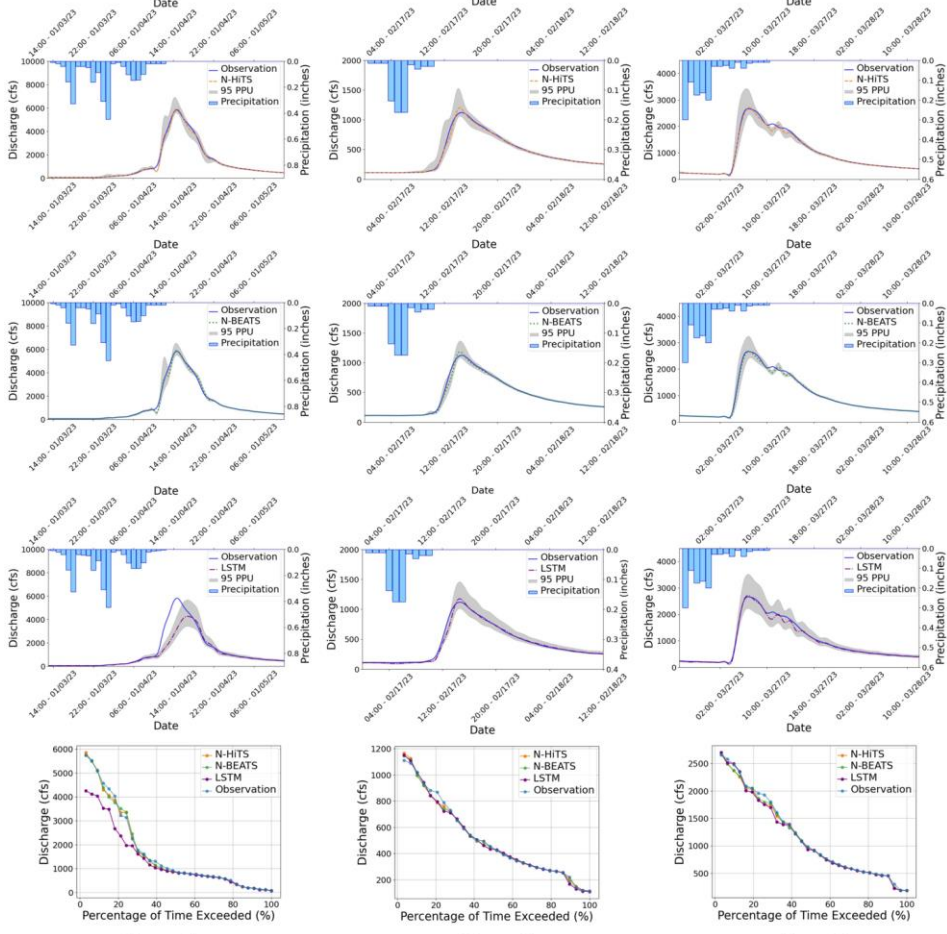
Table 4. **Accuracy and uncertainty** The performance metrics for the Killian Creek flood predictions.

Model	Performance Metric	Event 4	Event 5	Event 6
	NSE	<u>0.99.08 %1</u>	<u>0.97.13 %</u>	<u>0.99.08 %1</u>
	Persistent-NSE	<u>0.885</u>	<u>0.806</u>	<u>0.844</u>
	KGE	<u>0.982</u>	<u>0.967</u>	<u>0.991</u>
	RMSE	28.8	46.0	19.0
N-HITS	MAE	17.9	23.8	11.5
	PFE	0.017	0.008	0.020
	TPE (hours)	0	0	0
	P-Factor	92.6 %	90.9 %	100 %
	R-Factor	0.39	0.48	0.45
	NSE	<u>0.99.26 %</u>	<u>0.97.36 %</u>	<u>0.98.96 %</u>
	Persistent-NSE	<u>0.908</u>	<u>0.821</u>	<u>0.823</u>
	KGE	<u>0.972</u>	<u>0.951</u>	<u>0.973</u>
N-BEATS	RMSE	25.7	44.2	20.2
	MAE	18.3	25.9	14.0
	PFE	0.006	0.008	0.019
	TPE (hours)	0	0	0

	P-Factor	96.3 %	86.3 %	96.9 %
	R-Factor	0.43	0.53	0.43
	NSE	0.952	0.892	0.935
	Persistent-NSE	0.4	0.27	0.087
	KGE	<u>0.92</u>	<u>0.899</u>	<u>0.901</u>
	RMSE	65.7	89.2	50.3
LSTM	MAE	41.1	45	35.9
	PFE	0.031	0.058	0.098
	TPE (hours)	1	0	0
	P-Factor	70.4 %	72.73 %	<u>9081.829</u> %
	R-Factor	0.66	0.7	0.65

678

679



Event 1

Event 2

Event 3

Figure 7. 95 PPU band and FDC plots of N-HiTS, N-BEATS, and LSTM models for the three selected flooding events in the Lower Dog River gauging station.

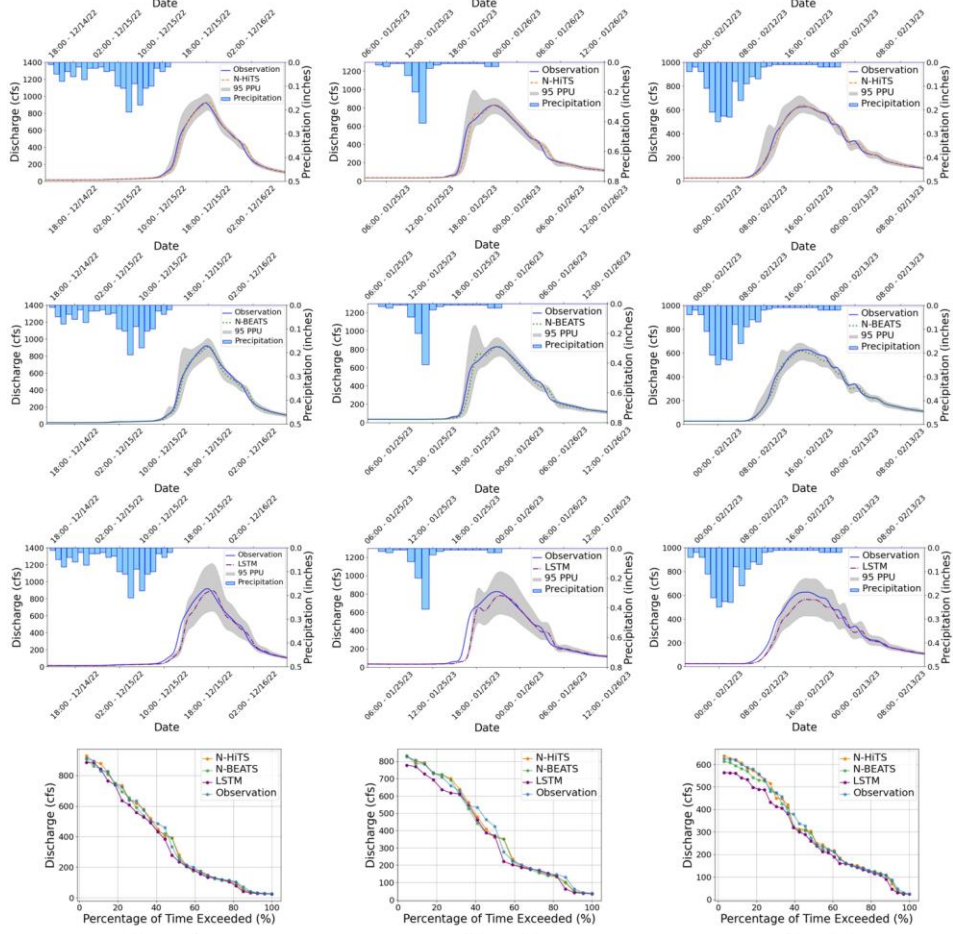
680

681

682

683

684



685
686
687

Figure 8. 95 PPU band and FDC plots of N-HiTS, N-BEATS, and LSTM models for the three selected flooding events in the Killian Creek gauging station.

688 Furthermore, in our investigation, we conducted an analysis to assess the impact of varying input sizes on
689 the performance of the N-HiTS, as the best model. We implemented four different durations as input sizes
690 to observe the corresponding differences in modeling performance. Notably, one of the key metrics affected
691 by changes in input size was 95PPU, which exhibited a general decrease with increasing input size.

692 As detailed in Table 5, we observed a discernible trend in the R-Factor of the N-HiTS model as the input
693 size was increased. Specifically, there was a ~~decrease~~ decline in the R-Factor as the input size expanded.

694 This trend underscores the influence of input size on model performance, particularly in terms of 95PPU
695 band and accuracy.

696 Overall, uncertainty analysis revealed that the integration of coupling MLE with N-HiTS and N-BEATS
697 models demonstrated superior performance in generating 95PPU, effectively reducing errors in flood
698 prediction. The MLE approach was more successful in reducing 95PPU bands of N-HiTS and N-BEATS
699 models compared to the LSTM, as indicated by the R-factor Factor and P-factor Factor. The N-BEATS
700 model demonstrated a narrower uncertainty band (lower R-factor Factor value), while the N-HiTS model
701 provided higher precision. Furthermore, incorporating data with various sizes into the N-HiTS model led
702 to a a reduction in narrower 95PPU and an improvement in the R-Factor, highlighting the significance of
703 input size in enhancing model accuracy and reducing prediction-uncertainty.

Formatted: Not Highlight

Table 5. N-HiTS's R-Factor results for three storm events in each case study, using 1 hour, 2 hours, 12 hours, and 24 hours input size in training.

Input Size	1 hour	6 hours	12 hours	24 hours
Dog River, GA - Event 1	0.314	0.337	0.29	0.272
Dog River, GA - Event 2	0.35	0.413	0.403	0.402
Dog River, GA - Event 3	0.358	0.459	0.374	0.336
Killian Creek, NC - Event 4	0.491	0.422	0.426	0.388
Killian Creek, NC - Event 5	0.584	0.503	0.557	0.483
Killian Creek, NC - Event 6	0.482	0.42	0.446	0.454

704

705 3.4. Sensitivity Analysis

706 In this study, we conducted a comprehensive sensitivity analysis of the N-HiTS, N-BEATS, and LSTM
707 models to evaluate their responsiveness to meteorological variables, specifically precipitation, humidity,
708 and temperature. The goal was to assess how the omission of input parameters impacts the overall
709 modeling performance compared to their full-variable counterparts.

710 To execute this analysis, we systematically trained each model by excluding meteorological variables one
711 or more at a time, subsequently evaluating their predictive performance using the entire testing dataset.
712 The results of our analysis indicated that N-HiTS and N-BEATS models exhibited minimal sensitivity to
713 meteorological variables, as evidenced by the negligible impact on their performance metric (i.e., NSE,
714 Persistent-NSE, KGE, RMSE, and MAE) upon parameter exclusion.

715 Notably, as shown in Table 6, the performance of the N-HiTS model displayed a marginal deviation
716 under variable omission, while the N-BEATS model exhibited consistent performance irrespective of the

Formatted: Font: Not Bold

717 inclusion or exclusion of meteorological variables. The structure of this algorithm is based on backward
 718 and forward residual links for univariate time series point forecasting which does not take into account
 719 other parameters in the prediction task. These findings suggest that the predictive capabilities of N-HiTS
 720 and N-BEATS models predominantly rely on historical flood data. They Both models demonstrated strong
 721 performance even without incorporating precipitation, temperature, or humidity data, underscoring their
 722 resilience ability in flood prediction in the absence of specific meteorological inputs. This resilience to
 723 meteorological variability capability underscores the robustness of the N-HiTS and N-BEATS models,
 724 positioning them as viable tools and perhaps appropriate for real-time flood forecasting tasks where direct
 725 meteorological data may be limited or unavailable.

726

727 Table 6. NSE Performance metrics values for N-HiTS, and N-BEATS, and LSTM models by excluding
 728 meteorological variables one or more at a time.

Model	Excluded Variables	NSE	Persistent-NSE	KGE	RMSE	MAE	Formatted Table
N-HiTS	Using all variables	0.99-655 %	0.92	0.988	22.66	4.19	Formatted: Space After: 12 pt, Line spacing: single
	Without Precipitation	0.99-34 %	0.91	0.97	23.28	4.31	Formatted: Space After: 12 pt, Line spacing: single
	Without Humidity	0.99-51 %	0.914	0.976	22.87	4.22	Formatted: Space After: 12 pt, Line spacing: single
	Without Temperature	0.99-549 %	0.921	0.985	22.43	4.14	Formatted: Space After: 12 pt
	Discharge only prediction	0.99-3 %	0.911	0.972	23.21	4.29	Formatted: Space After: 12 pt, Line spacing: single
N-BEATS	Using all variables	0.99-42 %	0.978	0.992	11.80	2.13	Formatted: Space After: 12 pt, Line spacing: single
	Without Precipitation	0.99-42 %	0.978	0.991	11.86	2.17	Formatted: Space After: 12 pt, Line spacing: single
	Without Humidity	0.99-42 %	0.978	0.991	11.81	2.16	Formatted: Space After: 12 pt, Line spacing: single
	Without Temperature	0.99-42 %	0.978	0.991	11.82	2.16	Formatted: Space After: 12 pt
	Discharge only prediction	0.99-42 %	0.978	0.991	11.96	2.17	Formatted: Space After: 12 pt, Line spacing: single
Using all variables		0.99-2 %	0.865	0.926	29.52	8.15	Formatted: Space After: 12 pt, Line spacing: single

LSTM	Without Precipitation	<u>0.9793 %</u>	<u>0.665</u>	<u>0.892</u>	<u>39.46</u>	<u>19.83</u>	← Formatted: Space After: 12 pt, Line spacing: single
	Without Humidity	<u>0.9913 %</u>	<u>0.843</u>	<u>0.925</u>	<u>31.73</u>	<u>9.15</u>	← Formatted: Space After: 12 pt, Line spacing: single
	Without Temperature	<u>0.98327 %</u>	<u>0.628</u>	<u>0.872</u>	<u>48.95</u>	<u>11.49</u>	← Formatted: Space After: 12 pt ← Formatted: Space After: 12 pt, Line spacing: single
	Discharge only prediction	<u>0.976 %</u>	<u>0.576</u>	<u>0.692</u>	<u>52.28</u>	<u>33.5</u>	← Formatted: Space After: 12 pt, Line spacing: single

729

730 **3.5 Computational Efficiency**

731 The computational efficiency of the N-HiTS, N-BEATS, and LSTM models, as well as a comparative
 732 analysis, is presented in Table 7. The study encompassed the entire process of training and predicting over
 733 the testing period, employing the optimized hyperparameters as previously described. Regarding the
 734 training time, it is noteworthy that the LSTM model exhibited the quickest performance. Specifically,
 735 LSTM demonstrated a training time that was 71% faster than N-HiTS and 93% faster than N-BEATS in
 736 the Lower Dog River watershed, while it was respectively, 126% and 118% faster than N-HiTS and N-
 737 BEATS in the Upper Dutchmans Creek, over training dataset. This is because LSTM has a simple
 738 architecture compared to the N-BEATS and N-HiTS and does not require multivariate features, hierarchical
 739 interpolation, and multi-rate data sampling. Perhaps, this outcome underscores the computational advantage
 740 of LSTM over other algorithms.

741 Conversely, during the testing period, the N-HiTS model emerged as the fastest and delivered the most
 742 efficient results in comparison to the other models. Notably, N-HiTS displayed a predicting time that was
 743 33% faster than LSTM and 32% faster than N-BEATS. This finding highlights the computational efficiency
 744 of the N-HiTS model in the context of predicting processes. Our experiments unveiled an interesting
 745 contrast in the computational performance of these models. While LSTM excelled in terms of training time,
 746 it lagged behind when it came to the testing period.

747 In the grand scheme of computational efficiency, model accuracy, and uncertainty analysis results, it
 748 becomes evident that the superiority of the N-HiTS and N-BEATS models in terms of accuracy and
 749 uncertainty analysis holds paramount importance. This significance is accentuated by the critical nature of
 750 flood prediction, where precision and certainty are pivotal. Therefore, computational efficiency must be
 751 viewed in the context of the broader objectives, with the accuracy and reliability of flood predictions taking
 752 precedence in ensuring the safety and preparedness of the affected regions.

753

754 Table 7. Computational costs of N-HiTS, N-BEATS, and LSTM models in the Dog River and Killian
 755 Creek gauging stations.

Model	Training Time over Train Datasets		Predicting Time over Test Datasets	
	Lower Dog River	Upper Dutchmans Creek	Lower Dog River	Upper Dutchmans Creek
N-HiTS	256.032	374.569	1533.029	1205.526
N-BEATS	288.511	361.599	2028.068	1482.305
LSTM	149.173	165.827	2046.140	1792.444

756

757 **4. Conclusion**

758 This study examined multiple NN algorithms for flood prediction. We selected two headwater streams with
 759 minimal human impacts to understand how NN approaches can capture flood magnitude and timing for
 760 these natural systems. In conclusion, our study represents a pioneering effort in exploring and advancing
 761 the application of NN algorithms, specifically the N-HiTS and N-BEATS models, in the field of flood
 762 prediction. In our case studies, both N-HiTS and N-BEATS models achieved state-of-the-art results,
 763 outperforming LSTM as a recurrent benchmark model, particularly in one-hour prediction. While a one-
 764 hour lead time may seem brief, it is highly significant for accurate flash flood prediction particularly in
 765 headwater streams an area with a proximity to large metropolitan cities, where rapid response is critical.
 766 These benchmarking results are arguably a pivotal part of this paper research. However, the N-BEATS
 767 model slightly emerged as a powerful and interpretable tool for flood prediction in most selected events.
 768 In addition, the results of the experiments described above demonstrated that N-HiTS multi-rate input
 769 sampling and hierarchical interpolation along with N-BEATS interpretable configuration are effective in
 770 learning location-specific runoff generation behaviors. Both algorithms with an MLP-based deep neural
 771 architecture with backward and forward residual links can sequentially project the data signal into
 772 polynomials and harmonic basis needed to predict intense storm behaviors with varied magnitudes. The
 773 innovation in this study – besides benchmarking the LSTM model for headwater streams – was to tackle
 774 volatility and memory complexity challenges, by locally specializing flood sequential predictions into the
 775 data signal's frequencies with interpretability, and hierarchical interpolation and pooling. Both N-HiTS and
 776 N-BEATS models offered similar performance as compared with the LSTM but also offered a level of
 777 interpretability about how the model learns to differentiate aspects of complex watershed-specific behaviors
 778 via data. The interpretability of N-HiTS and N-BEATS models stems from their designs. N-HiTS aims to
 779 enhance the accuracy of long-term time-series forecasts through hierarchical interpolation and multi-scale

780 data sampling, allowing it to focus on different data ~~aspects~~patterns, which prioritizes features essential ~~for~~
781 ~~to understand flood trends, i.e., larger scale magnitudes.~~ N-BEATS leverages interpretable configurations
782 ~~with trend and seasonality projections, enabling it to decompose time series data into intuitive components.~~
783 ~~N-BEATS~~ interpretable architecture is recommended for scarce data settings (such as flooding event), as it
784 regularizes its predictions through projections unto harmonic and trend basis. These approaches improve
785 model transparency by allowing understanding of how each part of the model contributes to the final
786 prediction, particularly when applied to complex flood patterns. Both models also support multivariate
787 series (and covariates) by flattening the model inputs to a 1-D series and reshaping the outputs to a tensor
788 of appropriate dimensions. This approach provides flexibility to handle arbitrary numbers of features.
789 Furthermore, both N-HiTS and N-BEATS models also support producing probabilistic predictions by
790 specifying a likelihood parameter. In terms of sensitivity analysis, both N-HiTS and N-BEATS models
791 maintain consistent performance even when trained without specific meteorological inputs. ~~Although,~~
792 ~~during some flashy floods, the models encountered challenges in capturing the peak flows and the dynamics~~
793 ~~of the recession curve, which is directly related to groundwater contribution to flood hydrograph, both~~
794 ~~models are~~were technically insensitive to rainfall data as an input variable. ~~This~~suggesting the fact that
795 ~~they both algorithms can learn discharge patterns in discharge data (which inherently include precipitation~~
796 ~~effects) without requiring meteorological data in input.~~ This ~~resilience~~ability underscores these models' ~~ability~~
797 ~~robustness in to generate~~generating accurate predictions using historical flood data alone, making them
798 valuable tools for flood prediction, especially in data-poor watersheds or even for real-time flood prediction
799 when near real-time meteorological inputs are limited or unavailable. In terms of computational efficiency,
800 both N-HiTS and N-BEATS are trained almost at the same pace; however, N-HiTS predicted the test data
801 much quicker than N-BEATS. Unlike N-HiTS and N-BEATS, LSTM excelled in reducing training time
802 due to its simplicity and limited number of parameters.
803 Moving forward, it is worth mentioning that predicting the magnitude of the recession curve of flood
804 hydrographs was particularly challenging for all models. We argue that this is because the relation between
805 base flow and time is particularly hard to calibrate due to ground-water effluent that is controlled by
806 geological and physical conditions (vegetation, wetlands, wet meadows) in headwater streams. In addition,
807 the situations of runoff occurrence are diverse and have a high measurement variance with high frequency
808 that can make it difficult for ~~NN~~the algorithms to fully capture discrete representation learning on time
809 series.
810 In future studies, it will be important to develop strategies to derive analogs to the interpretable
811 configuration as well as multi-rate input sampling, hierarchical interpolation, and backcast residual
812 connections that allow for the dynamic representation of flood times series data with different frequencies
813 and nonlinearity. A dynamic representation of flood time series is, at least in principle, possible by

814 generating additive predictions in different bands of the time-series signals, reducing memory footprint and
815 compute time, and improving architecture parsimony and accuracy. This would allow the model to “learn”
816 interpretability and hierarchical representations from raw data to reduce complexity as the information
817 flows through the network. Moreover, it is noteworthy that while a single station offers valuable localized
818 data, particularly for smaller watersheds such as headwater streams where runoff is closely tied to
819 immediate meteorological conditions, it may not fully capture the spatial heterogeneity of larger
820 watersheds. For our specific case, the methods applied effectively herein captured significant runoff
821 magnitude and flood dynamics in these small watersheds using a single station. However, we
822 recognize that for broader areas, incorporating spatially distributed data would likely enhance model
823 accuracy. Lastly, one could explore the idea of enhancing N-HiTS and N-BEATS (or NN algorithms, in
824 general) performance with uncertainty quantification by using more robust Bayesian inference such as
825 Bayesian Model Averaging (BMA) with fixed and flexible prior distributions (see Samadi et al., 2020)
826 and/or Markov Chain Monte-Carlo optimization methods (Duane et al., 1987) addressing both aleatoric and
827 epistemic uncertainties. We leave these approaches for future discussion and exploration in the context of
828 flood neural time series prediction.
829

830 **5. Acknowledgements**

831 This research is supported by the US National Science Foundation Directorate of Engineering (Grant #
832 CMMI 2125283). All opinions, findings, and conclusions or recommendations expressed in this material
833 are those of the authors and do not necessarily reflect the views of the NSF. The authors acknowledge and
834 appreciate Thorsten Wagener (University of Potsdam, Germany) discussion and feedback on
835 this manuscript. Clemson University (USA) is acknowledged for generous allotment of computing time on
836 the Palmetto cluster.
837

Formatted: Font: 11 pt

838 **6. Open Research**

839 The historical discharge data used in this study are from the USGS
840 (https://waterdata.usgs.gov/nwis/uv/?referred_module=sw), meteorological data from USDA
841 (<https://www.ncdc.noaa.gov/cdo-web/datatools/lcd>). We have uploaded the datasets and codes
842 used in this research to Zenodo, accessible via <https://zenodo.org/records/13343364>. For
843 modeling, we used the NeuralForecast package (Olivares et al., 2022), available at:
844 <https://github.com/Nixtla/neuralforecast>.
845

846 **7. References**

847 Abbaspour, K.C., Yang, J., Maximov, I., Siber, R., Bogner, K., Mieleitner, J., Zobrist, J., Srinivasan, R.,
848 2007. Modelling hydrology and water quality in the pre-alpine/alpine Thur watershed using SWAT.
849 *Journal of Hydrology* 333, 413–430. <https://doi.org/10.1016/j.jhydrol.2006.09.014>

850 Alaa, A.M., van der Schaar, M., 2019. Attentive State-Space Modeling of Disease Progression, in:
851 *Advances in Neural Information Processing Systems*. Curran Associates, Inc.

852 Asquith, W.H., Roussel, M.C., Thompson, D.B., Cleveland, T.G., Fang, X., 2005. Summary of
853 dimensionless Texas hyetographs and distribution of storm depth developed for Texas Department
854 of Transportation research project 0–4194 (No. 0–4194–4). Texas Department of Transportation.

855 Barnard, P.L., van Ormondt, M., Erikson, L.H., Eshleman, J., Hapke, C., Ruggiero, P., Adams, P.N.,
856 Foxgrover, A.C., 2014. Development of the Coastal Storm Modeling System (CoSMoS) for
857 predicting the impact of storms on high-energy, active-margin coasts. *Nat Hazards* 74, 1095–1125.
858 <https://doi.org/10.1007/s11069-014-1236-y>

859 Basso, S., Schirmer, M., Botter, G., 2016. A physically based analytical model of flood frequency curves.
860 *Geophysical Research Letters* 43, 9070–9076. <https://doi.org/10.1002/2016GL069915>

861 Challu, C., Olivares, K.G., Oreshkin, B.N., Garza, F., Mergenthaler-Canseco, M., Dubrawski, A., 2022.
862 N-HiTS: Neural Hierarchical Interpolation for Time Series Forecasting.
863 <https://doi.org/10.48550/arXiv.2201.12886>

864 Chen, Y., Li, J., Xu, H., 2016. Improving flood forecasting capability of physically based distributed
865 hydrological models by parameter optimization. *Hydrology and Earth System Sciences* 20, 375–
866 392. <https://doi.org/10.5194/hess-20-375-2016>

867 Clark, M.P., Nijssen, B., Lundquist, J.D., Kavetski, D., Rupp, D.E., Woods, R.A., Freer, J.E., Gutmann,
868 E.D., Wood, A.W., Brekke, L.D., Arnold, J.R., Gochis, D.J., Rasmussen, R.M., 2015. A unified
869 approach for process-based hydrologic modeling: 1. Modeling concept. *Water Resources Research*
870 51, 2498–2514. <https://doi.org/10.1002/2015WR017198>

871 CRED, n.d. EM-DAT - The international disaster database [WWW Document]. URL
872 <https://www.emdat.be/> (accessed 6.5.24).

873 Dasgupta, A., Arnal, L., Emerton, R., Harrigan, S., Matthews, G., Muhammad, A., O'Regan, K., Pérez-
874 Ciria, T., Valdez, E., van Osnabrugge, B., Werner, M., Buontempo, C., Cloke, H., Pappenberger,
875 F., Pechlivanidis, I.G., Prudhomme, C., Ramos, M.-H., Salamon, P., n.d. Connecting hydrological
876 modelling and forecasting from global to local scales: Perspectives from an international joint
877 virtual workshop. *Journal of Flood Risk Management* n/a, e12880.
878 <https://doi.org/10.1111/jfr3.12880>

879 Defontaine, T., Ricci, S., Lapeyre, C., Marchandise, A., Pape, E.L., 2023. Flood forecasting with Machine
880 Learning in a scarce data layout. *IOP Conf. Ser.: Earth Environ. Sci.* 1136, 012020.
881 <https://doi.org/10.1088/1755-1315/1136/1/012020>

882 Duane, S., Kennedy, A.D., Pendleton, B.J., Roweth, D., 1987. Hybrid Monte Carlo. Physics Letters B
883 195, 216–222. [https://doi.org/10.1016/0370-2693\(87\)91197-X](https://doi.org/10.1016/0370-2693(87)91197-X)

884 Erikson, L.H., Espejo, A., Barnard, P.L., Serafin, K.A., Hegermiller, C.A., O'Neill, A., Ruggiero, P.,
885 Limber, P.W., Mendez, F.J., 2018. Identification of storm events and contiguous coastal sections
886 for deterministic modeling of extreme coastal flood events in response to climate change. Coastal
887 Engineering 140, 316–330. <https://doi.org/10.1016/j.coastaleng.2018.08.003>

888 Evin, G., Le Lay, M., Fouchier, C., Mas, A., Colleoni, F., Penot, D., Garambois, P.-A., Laurantin, O.,
889 2023. Evaluation of hydrological models on small mountainous catchments: impact of the
890 meteorological forcings. <https://doi.org/10.5194/egusphere-2023-845>

891 Fan, C., Zhang, Y., Pan, Y., Li, X., Zhang, C., Yuan, R., Wu, D., Wang, W., Pei, J., Huang, H., 2019.
892 Multi-Horizon Time Series Forecasting with Temporal Attention Learning, in: Proceedings of the
893 25th ACM SIGKDD International Conference on Knowledge Discovery & Data Mining, KDD '19.
894 Association for Computing Machinery, New York, NY, USA, pp. 2527–2535.
895 <https://doi.org/10.1145/3292500.3330662>

896 Fang, K., Kifer, D., Lawson, K., Shen, C., 2020. Evaluating the Potential and Challenges of an
897 Uncertainty Quantification Method for Long Short-Term Memory Models for Soil Moisture
898 Predictions. Water Resources Research 56, e2020WR028095.
899 <https://doi.org/10.1029/2020WR028095>

900 Global assessment report on disaster risk reduction 2015 | UNDRR, 2015. URL:
901 <http://www.undrr.org/publication/global-assessment-report-disaster-risk-reduction-2015> (accessed
902 6.5.24).

903 Gotvald, A.J., 2010. Historic flooding in Georgia, 2009: U.S. Geological Survey Open-File Report 2010–
904 1230, 19 p.

905 Gupta, H.V., Kling, H., Yilmaz, K.K., Martinez, G.F., 2009. Decomposition of the mean squared error
906 and NSE performance criteria: Implications for improving hydrological modelling. Journal of
907 Hydrology 377, 80–91. <https://doi.org/10.1016/j.jhydrol.2009.08.003>

908 Hochreiter, S., Younger, A.S., Conwell, P.R., 2001. Learning to Learn Using Gradient Descent, in:
909 Dorffner, G., Bischof, H., Hornik, K. (Eds.), Artificial Neural Networks — ICANN 2001. Springer,
910 Berlin, Heidelberg, pp. 87–94. https://doi.org/10.1007/3-540-44668-0_13

911 Hsu, K., Gupta, H.V., Sorooshian, S., 1995. Artificial Neural Network Modeling of the Rainfall-Runoff
912 Process. Water Resources Research 31, 2517–2530. <https://doi.org/10.1029/95WR01955>

913 Jonkman, S.N., 2005. Global Perspectives on Loss of Human Life Caused by Floods. Nat Hazards 34,
914 151–175. <https://doi.org/10.1007/s11069-004-8891-3>

915 Kingma, D.P., Ba, J., 2017. Adam: A Method for Stochastic Optimization.
916 <https://doi.org/10.48550/arXiv.1412.6980>

917 Kratzert, F., Klotz, D., Brenner, C., Schulz, K., Herrnegger, M., 2018. Rainfall–runoff modelling using
918 Long Short-Term Memory (LSTM) networks. *Hydrology and Earth System Sciences* 22, 6005–
919 6022. <https://doi.org/10.5194/hess-22-6005-2018>

920 Lim, B., Arik, S.Ö., Loeff, N., Pfister, T., 2021. Temporal Fusion Transformers for interpretable multi-
921 horizon time series forecasting. *International Journal of Forecasting* 37, 1748–1764.
922 <https://doi.org/10.1016/j.ijforecast.2021.03.012>

923 Lobligeois, F., Andréassian, V., Perrin, C., Tabary, P., Loumagne, C., 2014. When does higher spatial
924 resolution rainfall information improve streamflow simulation? An evaluation using 3620 flood
925 events. *Hydrology and Earth System Sciences* 18, 575–594. <https://doi.org/10.5194/hess-18-575-2014>

927 MacDonald, L.H., Coe, D., 2007. Influence of Headwater Streams on Downstream Reaches in Forested
928 Areas. *Forest Science* 53, 148–168. <https://doi.org/10.1093/forestscience/53.2.148>

929 Martinaitis, S.M., Wilson, K.A., Yussouf, N., Gourley, J.J., Vergara, H., Meyer, T.C., Heinselman, P.L.,
930 Gerard, A., Berry, K.L., Vergara, A. and Monroe, J., 2023. A path toward short-term probabilistic
931 flash flood prediction. *Bulletin of the American Meteorological Society*, 104(3), pp.E585-E605.

932 McCallum, B.E., and Gotvald, A.J., 2010, Historic flooding in northern Georgia, September 16–22, 2009:
933 U.S. Geological Survey Fact Sheet 2010–3061, 4 p.

934 McCuen, R.H., Knight, Z., Cutter, A.G., 2006. Evaluation of the Nash–Sutcliffe Efficiency Index. *Journal*
935 *of Hydrologic Engineering* 11, 597–602. [https://doi.org/10.1061/\(ASCE\)1084-0699\(2006\)11:6\(597\)](https://doi.org/10.1061/(ASCE)1084-0699(2006)11:6(597)

937 Munn, M., Sheibley, R., Waite, I., Meador, M., 2020. Understanding the relationship between stream
938 metabolism and biological assemblages. *Freshwater Science* 39, 680–692.
939 <https://doi.org/10.1086/711690>

940 Nash, J.E., Sutcliffe, J.V., 1970. River flow forecasting through conceptual models part I — A discussion
941 of principles. *Journal of Hydrology* 10, 282–290. [https://doi.org/10.1016/0022-1694\(70\)90255-6](https://doi.org/10.1016/0022-1694(70)90255-6)

942 Nevo, S., Morin, E., Gerzi Rosenthal, A., Metzger, A., Barshai, C., Weitzner, D., Voloshin, D., Kratzert,
943 F., Elidan, G., Dror, G., Begelman, G., Nearing, G., Shalev, G., Noga, H., Shavitt, I., Yuklea, L.,
944 Royz, M., Giladi, N., Peled Levi, N., Reich, O., Gilon, O., Maor, R., Timnat, S., Shechter, T.,
945 Anisimov, V., Gigi, Y., Levin, Y., Moshe, Z., Ben-Haim, Z., Hassidim, A., Matias, Y., 2022. Flood
946 forecasting with machine learning models in an operational framework. *Hydrology and Earth*
947 *System Sciences* 26, 4013–4032. <https://doi.org/10.5194/hess-26-4013-2022>

948 NRCS (2009). Part 630 Hydrology National Engineering Handbook, Chapter 15: Time of Concentration.

949 Olivares, K. G., Challú, C., Garza, F., Mergenthaler Canseco, M., & Dubrawski, A. (2022).
950 *NeuralForecast: User friendly state-of-the-art neural forecasting models*. PyCon Salt Lake City,
951 Utah, US 2022. Retrieved from <https://github.com/Nixtla/neuralforecast>

952 Olivares, K.G., Meetei, O.N., Ma, R., Reddy, R., Cao, M., Dicker, L., 2024. Probabilistic hierarchical
953 forecasting with deep Poisson mixtures. *International Journal of Forecasting* 40, 470–489.
954 <https://doi.org/10.1016/j.ijforecast.2023.04.007>

955 Oreshkin, B.N., Carpov, D., Chapados, N., Bengio, Y., 2020. N-BEATS: Neural basis expansion analysis
956 for interpretable time series forecasting. <https://doi.org/10.48550/arXiv.1905.10437>

957 Pally, R.J., Samadi, V., 2021. Application of image processing and convolutional neural networks for
958 flood image classification and semantic segmentation. *Environmental Modelling & Software* 148,
959 105285. <https://doi.org/10.1016/j.envsoft.2021.105285>

960 Palmer, T.N., 2012. Towards the probabilistic Earth-system simulator: a vision for the future of climate
961 and weather prediction. *Quarterly Journal of the Royal Meteorological Society* 138, 841–861.
962 <https://doi.org/10.1002/qj.1923>

963 Park, K., Lee, E.H., 2024. Urban flood vulnerability analysis and prediction based on the land use using
964 Deep Neural Network. *International Journal of Disaster Risk Reduction* 101, 104231.
965 <https://doi.org/10.1016/j.ijdrr.2023.104231>

966 Pourreza-Bilondi, M., Samadi, S.Z., Akhond-Ali, A.-M., Ghahraman, B., 2017. Reliability of Semiarid
967 Flash Flood Modeling Using Bayesian Framework. *Journal of Hydrologic Engineering* 22,
968 05016039. [https://doi.org/10.1061/\(ASCE\)HE.1943-5584.0001482](https://doi.org/10.1061/(ASCE)HE.1943-5584.0001482)

969 Refsgaard, J.C., Stisen, S., Koch, J., 2022. Hydrological process knowledge in catchment modelling –
970 Lessons and perspectives from 60 years development. *Hydrological Processes* 36, e14463.
971 <https://doi.org/10.1002/hyp.14463>

972 Roelvink, D., Reniers, A., van Dongeren, A., van Thiel de Vries, J., McCall, R., Lescinski, J., 2009.
973 Modelling storm impacts on beaches, dunes and barrier islands. *Coastal Engineering* 56, 1133–
974 1152. <https://doi.org/10.1016/j.coastaleng.2009.08.006>

975 Russo, S., Perraquin, N., Stalder, S., Perez-Cruz, F., Leitao, J.P., Obozinski, G., Wegner, J.D., 2023. An
976 evaluation of deep learning models for predicting water depth evolution in urban floods.
977 <https://doi.org/10.48550/arXiv.2302.10062>

978 Safaei-Moghadam, A., Tarboton, D., Minsker, B., 2023. Estimating the likelihood of roadway pluvial
979 flood based on crowdsourced traffic data and depression-based DEM analysis. *Natural Hazards and*
980 *Earth System Sciences* 23, 1–19. <https://doi.org/10.5194/nhess-23-1-2023>

981 Saksena, S., Dey, S., Merwade, V., Singhofen, P.J., 2020. A Computationally Efficient and Physically
982 Based Approach for Urban Flood Modeling Using a Flexible Spatiotemporal Structure. *Water*
983 *Resources Research* 56, e2019WR025769. <https://doi.org/10.1029/2019WR025769>

984 Samadi, S., Pourreza-Bilondi, M., Wilson, C. a. M.E., Hitchcock, D.B., 2020. Bayesian Model Averaging
985 With Fixed and Flexible Priors: Theory, Concepts, and Calibration Experiments for Rainfall-Runoff

986 Modeling. Journal of Advances in Modeling Earth Systems 12, e2019MS001924.
987 <https://doi.org/10.1029/2019MS001924>

988 Scott, J., n.d. Widespread Flooding After Severe Storms - WCCB Charlotte's CW. Available at:
989 <https://www.wccbcharlotte.com/2020/02/08/widespread-flooding-after-severe-storms/> (accessed
990 6.11.24).

991 Sukovich, E.M., Ralph, F.M., Barthold, F.E., Reynolds, D.W., Novak, D.R., 2014. Extreme Quantitative
992 Precipitation Forecast Performance at the Weather Prediction Center from 2001 to 2011. Weather
993 and Forecasting 29, 894–911. <https://doi.org/10.1175/WAF-D-13-00061.1>

994 Tabas, S.S., Samadi, S., 2022. Variational Bayesian dropout with a Gaussian prior for recurrent neural
995 networks application in rainfall–runoff modeling. Environ. Res. Lett. 17, 065012.
996 <https://doi.org/10.1088/1748-9326/ac7247>

997 Thompson, C.M., Frazier, T.G., 2014. Deterministic and probabilistic flood modeling for contemporary
998 and future coastal and inland precipitation inundation. Applied Geography 50, 1–14.
999 <https://doi.org/10.1016/j.apgeog.2014.01.013>

1000 Tiwari, M.K., Chatterjee, C., 2010. Development of an accurate and reliable hourly flood forecasting
1001 model using wavelet-bootstrap-ANN (WBANN) hybrid approach. Journal of Hydrology 394, 458–
1002 470. <https://doi.org/10.1016/j.jhydrol.2010.10.001>

1003 Watershed Report | Office of Water | US EPA, n.d. Available at:
1004 <https://watersgeo.epa.gov/watershedreport/?comid=9224629> (accessed 6.9.24).

1005 Wee, G., Chang, L.-C., Chang, F.-J., Mat Amin, M.Z., 2023. A flood Impact-Based forecasting system by
1006 fuzzy inference techniques. Journal of Hydrology 625, 130117.
1007 <https://doi.org/10.1016/j.jhydrol.2023.130117>

1008 Windheuser, L., Karanjit, R., Pally, R., Samadi, S., Hubig, N.C., 2023. An End-To-End Flood Stage
1009 Prediction System Using Deep Neural Networks. Earth and Space Science 10, e2022EA002385.
1010 <https://doi.org/10.1029/2022EA002385>

1011 Zafarmomen, N., Alizadeh, H., Bayat, M., Ehtiat, M., Moradkhani, H., 2024. Assimilation of Sentinel-
1012 Based Leaf Area Index for Modeling Surface-Ground Water Interactions in Irrigation Districts.
1013 Water Resources Research 60, e2023WR036080. <https://doi.org/10.1029/2023WR036080>

1014 Zhang, L., Qin, H., Mao, J., Cao, X., Fu, G., 2023. High temporal resolution urban flood prediction using
1015 attention-based LSTM models. Journal of Hydrology 620, 129499.
1016 <https://doi.org/10.1016/j.jhydrol.2023.129499>

1017 Zhang, Y., Pan, D., Griensven, J.V., Yang, S.X., Gharabaghi, B., 2023. Intelligent flood forecasting and
1018 warning: a survey. ir 3, 190–212. <https://doi.org/10.20517/ir.2023.12>

1019 Zou, Y., Wang, J., Lei, P., Li, Y., 2023. A novel multi-step ahead forecasting model for flood based on time
1020 residual LSTM. *Journal of Hydrology* 620, 129521. <https://doi.org/10.1016/j.jhydrol.2023.129521>

1021